NAVAL POSTGRADUATE SCHOOL
Monterey, California

THESIS

**SHALLOW WATER BATHYMETRY AT
LAKE TAHOE FROM AVIRIS DATA**

by

Thomas M. Fisher

December 1999

Thesis Co-Advisors: Richard C. Olsen
                                                  Pierre-Marie Poulain

REPORT DOCUMENTATION PAGE

Form Approved
OMB No. 0704-0188

1. AGENCY USE ONLY *(Leave blank)*	2. REPORT DATE December 1999	3. REPORT TYPE AND DATES COVERED Master's Thesis

4. TITLE AND SUBTITLE
SHALLOW WATER BATHYMETRY AT LAKE TAHOE FROM AVIRIS DATA

5. FUNDING NUMBERS

6. AUTHOR(S)
Fisher, Thomas M.

7. PERFORMING ORGANIZATION NAME(S) AND ADDRESS(ES)
Naval Postgraduate School
Monterey, CA 93943-5000

8. PERFORMING ORGANIZATION REPORT NUMBER

9. SPONSORING / MONITORING AGENCY NAME(S) AND ADDRESS(ES)

10. SPONSORING / MONITORING AGENCY REPORT NUMBER

11. SUPPLEMENTARY NOTES
The views expressed in this thesis are those of the author and do not reflect the official policy or position of the Department of Defense or the U.S. Government.

12a. DISTRIBUTION / AVAILABILITY STATEMENT
Approved for public release; distribution is unlimited.

12b. DISTRIBUTION CODE

13. ABSTRACT *(maximum 200 words)*

One of the United States Navy Oceanographic community's roles is to keep an accurate worldwide database of oceanic bathymetry. In the littoral zones, much of the data is out of date or has not been done. Stuffle et al. (1996) utilized a method addressing shallow water areas using the Hyperspectral Digital Imagery Collection Experiment (HYDICE) sensor on a small region in Lake Tahoe. As a follow-on, this work used a different sensor, the Airborne Visible/InfraRed Imaging Spectrometer (AVIRIS) sensor, and covered a much larger area on the opposite side of the lake. Principle components analysis (PCA) of the region of interest (ROI) revealed nine spectrally unique water classes. *A priori* knowledge of one bottom type in this ROI allowed insertion of a known bottom reflectance spectrum into a derived computer algorithm that, using also diffuse attenuation coefficients from HYDROLIGHT and reflectance just below the water surface derived from AVIRIS data, allowed computation of the bottom depth. Results compared within 30% of depth from a USGS bathymetric chart. This method holds much promise in clear waters, and next needs to be tested in the coastal ocean environment.

14. SUBJECT TERMS
AVIRIS, Hyperspectral, Bathymetry, Lake Tahoe, Optical properties of water

15. NUMBER OF PAGES
56

16. PRICE CODE

17. SECURITY CLASSIFICATION OF REPORT Unclassified	18. SECURITY CLASSIFICATION OF THIS PAGE Unclassified	19. SECURITY CLASSIFI- CATION OF ABSTRACT Unclassified	20. LIMITATION OF ABSTRACT UL

i

**SHALLOW WATER BATHYMETRY AT LAKE TAHOE
FROM AVIRIS DATA**

Thomas M. Fisher
Lieutenant, United States Navy
B.S., Pennsylvania State University, 1991

Submitted in partial fulfillment of the
requirements for the degree of

MASTER OF SCIENCE IN AIR-OCEAN SCIENCES

from the

**NAVAL POSTGRADUATE SCHOOL
December 1999**

Author: _____

Thomas M. Fisher

Approved by: _____

Richard C. Olsen, Thesis Co-Advisor

_____

Pierre-Marie Poulain, Thesis Co-advisor

_____

Roland W.Garwood, Jr., Chairman
Department of Oceanography

ABSTRACT

One of the United States Navy Oceanographic community's roles is to keep an accurate worldwide database of oceanic bathymetry. In the littoral zones, much of the data is out of date or is unavailable. Stuffle et al. (1996) utilized a method addressing shallow water areas using the Hyperspectral Digital Imagery Collection Experiment (HYDICE) sensor on a small region in Lake Tahoe. As a follow-on, this work used a different sensor, the Airborne Visible/InfraRed Imaging Spectrometer (AVIRIS) sensor, and covered a much larger area on the opposite side of the lake.   Principle components analysis (PCA) of the region of interest (ROI) revealed nine spectrally unique water classes. *A priori* knowledge of one bottom type in this ROI allowed insertion of a known bottom reflectance spectrum into a derived computer algorithm that, using also diffuse attenuation coefficients from HYDROLIGHT and reflectance just below the water surface derived from AVIRIS data, allowed computation of the bottom depth. Results compared within 30% of depth from a USGS bathymetric chart. This method holds much promise in clear waters, and next needs to be tested in the coastal ocean environment.

THIS PAGE INTENTIONALLY LEFT BLANK

TABLE OF CONTENTS

I.   INTRODUCTION

The Meteorology and Oceanography Community (METOC) of the United States Navy is tasked with the role of obtaining, storing, and updating a worldwide database of ocean bathymetry, known as the Digital Bathymetric Data Base (DBDB). The Office of Naval Research uses the DBDB as an input for various modelling algorithms (acoustic prediction, tide and surf forecasting, weapon systems); for planning charts (command and control, mission planning, tactical decision aids); and for coastal zone management, environmental monitoring, engineering/construction, and resource development/exploration.

Many coastal areas of the world have never been fully surveyed, and many that have are seriously outdated. Stuffle et al. (1996) utilized a method addressing these shallow water areas using hyperspectral data collected over a small region of Lake Tahoe. This work consisted of isolating different "classes" of water, unmixing the various contributions to sensor radiance, inverting the radiative transfer equation, and solving for the water depth. As a follow-on, this work will apply a similar method using data collected from a different sensor and from a much larger area on the opposite side of the lake. The purpose is to assess the applicability of this method to a different and much larger region using a different sensor.

The problem. When a airborne or satellite sensor "looks" at a pixel of water on the earth, it "sees" upwelling irradiance. If broken down to values at each wavelength, and then plotted as a continuous curve across all of these wavelengths, a continuous radiance spectrum is created. This spectrum has a story to tell – it is a summation of contributions made by atmospheric backscattering, absorption by chlorophyll, bottom reflectance, etc. The problem is to unmix these various components, isolating each one. Theoretically, using the radiative

transfer equation, absorption and scattering in the water column under the pixel can then be determined.

The focus of this thesis is to determine the water depth, assuming other properties are known or can be estimated. These other properties can come from a variety of sources. For example, atmospheric radiative transfer models can provide sky radiance contributions; in-situ measurements can provide chlorophyll concentrations; etc. Once the above properties are known, the "inverse method" is applied, solving the radiative transfer equation for the desired variable.

Many years of research have gone into solving the many facets of this complex problem – after all, the variability of these parameters is tremendous in three-dimensional space and time in the littoral zone. Various algorithms are being tested, however none is "perfect" so far. The culmination of the Navy's efforts is going into the Hyperspectral Remote Sensing Technology (HRST) project, which is discussed briefly in Chapter IV. Only time will tell the accuracy and applicability of these methods to large-scale areas of the Earth's littoral zones.

What follows are background information, including the optical properties of water and the radiative transfer equation, (the problems unique to the coastal zone), and a depth-derivation scheme applied to a portion of Lake Tahoe. This is followed by a comparison of the output to a United States Geological Survey (USGS) bathymetry chart, possible error sources and limitations of this method, and a brief discussion on future endeavors and research.

II.   THE WATER COLUMN

Central to unmixing spectra seen over water is understanding how light is affected in the water column, meaning that volume or "column" of water under each pixel. Significant portions of Mobley (1994) are used in this section to provide background information on how light is affected in the water column.

A.   OPTICAL PROPERTIES OF WATER

All natural waters, especially the euphotic zone of littoral waters, show great variations in the nature and concentration of organisms, particulates, and dissolved substances. Hence these biological, geological, and chemical "bulk" properties will vary spatially and temporally. For convenience, these are divided into two distinct classes, inherent and apparent. A brief summary follows.

1. Inherent Optical Properties (IOPs).

These properties depend on the medium only, and are independent of the surrounding light field. There are numerous properties, but of particular interest are the spectral absorption and scattering coefficients. The spectral absorption coefficient, $a(\lambda)$, is the fraction of incident power at wavelength λ that is absorbed per unit distance in the medium. The spectral scattering coefficient, $b(\lambda)$, is the fractional part of the incident power per unit distance that is scattered out of the beam. Together, $a(\lambda)$ and $b(\lambda)$ sum to form the beam attenuation coefficient, $c(\lambda)$:

$$c(\lambda) = a(\lambda) + b(\lambda) \tag{2.1}$$

3

IOPs are measured from water samples and are difficult to measure in situ.

2. Apparent Optical Properties (AOPs).

These properties depend on both the medium and the directional structure of the surrounding light field. An AOP must also be independent of environmental parameters, such as sea state. There are several AOPs, but two are of particular importance to the bathymetry problem: spectral irradiance reflectance, $R_s(z;\mathbf{l})$, and spectral remote-sensing reflectance, R.

Spectral irradiance reflectance, $R_s(z;\mathbf{l})$, is the ratio of spectral upwelling to spectral downwelling irradiances across a horizontal plane, at a depth z:

$$R_s(z;\mathbf{l}) = \frac{E_u(z;\mathbf{l})}{E_d(z;\mathbf{l})} \qquad (2.2)$$

This parameter is usually evaluated at the water's surface, where $z = 0$. An associated parameter is the directional water leaving radiance, L.

Figure 2.1 pictorially represents the relationship between L, E_d, and E_u. The variable $\mathbf{q}$ represents the vertical angular displacement from a normal line to the plane, measured counterclockwise from the $-z$ direction; $\mathbf{f}$ is the horizontal angular displacement, measured counterclockwise from the $+x$ direction.

Spectral remote sensing reflectance, R, is the ratio of upwelling or "water-leaving" radiance, L_w, to spectral downwelling plane irradiance, E_d, evaluated just below the water's surface $(z = 0-)$:

$$R(0-)_{q,f;l} = \frac{L_w(z=0-;q,f;l)}{E_d(z=0-;l)}.$$
(2.3)

$R(0-)_{q,f;l}$ is merely a measure of what portion of the downwelling light, after penetrating the surface of the water and interacting with the constituents of the water column and bottom, is returned through the surface in the direction (q,f) so that (in this case) a hyperspectral sensor can detect it.
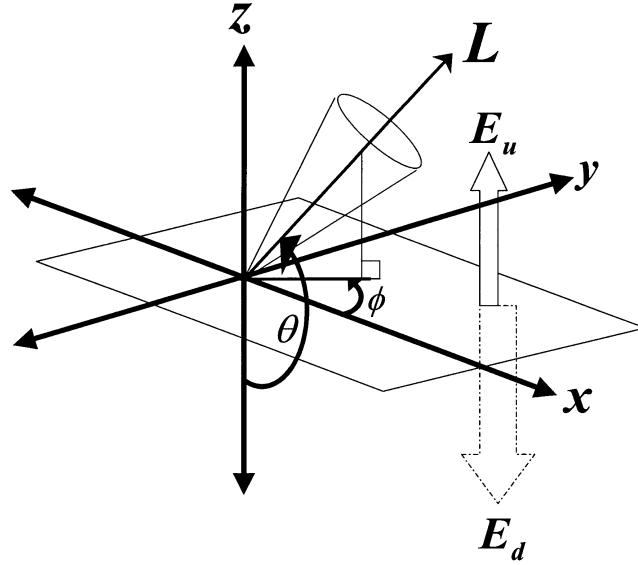

Figure 2.1. Pictoral representation of E_u, E_d, and L, in Relation to a horizontal plane. Note that L is merely E_u or E_d in one solid angle, (q,f).

B. SPECTRAL DIFFUSE ATTENUATION COEFFICIENT AND JERLOV WATER TYPES

Near the middle of the water column (away from the boundary effects of the surface and bottom), sunlight and sky radiances and irradiances decrease approximately exponentially with depth. Therefore the depth dependence of spectral downwelling irradiance, $E_d(z; \lambda)$, may be written as:

$$E_d(z; \lambda) = E_d(0; \lambda) e^{-\int_0^z 2K_d(z; \lambda)dz}$$
(2.4)

$K_d(z; \lambda)$ is the spectral diffuse attenuation coefficient for spectral downwelling plane radiance. Therefore,

$$K_d(z; \lambda) = -\frac{1}{E_d(z; \lambda)} \frac{dE_d(z; \lambda)}{dz}$$
(2.5)

Smith and Baker (1978) discuss some useful properties of K_d:

- K_d is strongly correlated with phytoplankton chlorophyll concentration, thus providing a connection between biology and the marine optical properties

- Approximately 90% of the diffusely reflected light from a water body comes from a surface layer of water of depth $\frac{1}{K_d}$

- K_d is related to AOPs, such as absorption coefficients, through the radiative transfer theory.

6

In homogeneous waters, K_d depends weakly on depth and therefore can serve as a good descriptor of the water body. K_d varies with wavelength over a wide range of waters, and for this reason is regarded as a "quasi-inherent optical property" – it is governed by changes in the water body IOPs and not by the external environment.

Jerlov (1976) developed a classification scheme for oceanic waters based on the spectral shape of K_d. Open-ocean waters are numbered I, IA, IB, II, and III; with type I being the clearest and type III being the most turbid. Coastal waters are numbered 1 through 9, with 1 being the clearest and 9 being the most turbid.

C.   CONSTITUENTS OF OPTICAL SIGNIFICANCE IN NATURAL WATERS

Natural waters are comprised of numerous organic and inorganic dissolved substances and particles. The size, type, and distribution of these particles make the bathymetry problem especially complex. A brief discussion of the particle types and their effects on visible light follow.

1. Dissolved substances

a) Salts

The average salinity of seawater is 35. These dissolved salts increase scattering by 30% over pure water, but have a negligible effect on absorption.

b) Organic compounds

Organic compounds found in water are called yellow matter, or CDOM (colored dissolved organic matter). They are produced from the decay of plant matter, and are generally brown in color and found in high concentration in the euphotic zone of littoral waters. CDOM is a significant absorber in the blue wavelengths of visible light, and becoming less absorbing toward the red.

2. Particulate matter

a) Inorganic

These particles appear in the water column from wind-blown dust, river outlets, or disturbing bottom sediments from currents or wave action. Inorganic particles consist mostly of finely ground quartz sand, metal oxides, and clay minerals. Depending on the concentration and distribution, these particles can have a nil effect on the ambient light field or can scatter light greatly.

b) Organic

Organic particles include viruses, colloids, bacteria, phytoplankton, organic detritus, and zooplankton. These particles again vary significantly in size, concentration, and distribution, but all of these except phytoplankton are major scatterers of visible light. Phytoplankton itself is a strong absorber in the blue and red, peaking at $\lambda = 430$ nm and $\lambda = 665$ nm. Therefore, phytoplankton is primarily responsible for determining the optical properties of most oceanic waters. Chlorophyll concentration essentially describes the sum

of chlorophyll pigments in phytoplankton. It varies from 0.01 mg/m^3 in the clearest open-ocean waters to 10 mg/m^3 in productive coastal upwelling regions, to 100 mg/m^3 in eutrophic estuaries or lakes. The global open-ocean average value is near 0.5 mg/m^3.

A clear representation of the effects of various water constituents is seen in the different spectral curves of Figure 2.2, which specifically show the variation in remote sensing reflectance just below the water surface, $R(0-)$, for various water types. Of particular note is the reflectance in the green/yellow and red bands for eutrophic waters.
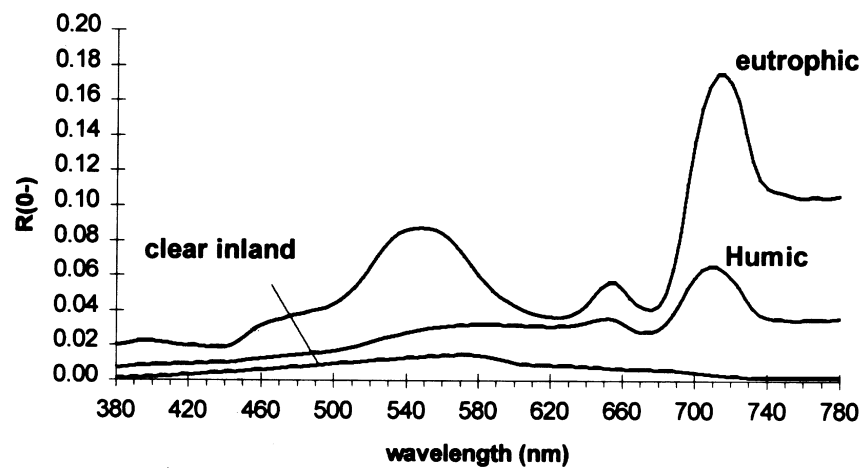

Figure 2.2. Figure 1 from Dekker et al. (1997), showing that eutrophic (plankton-rich) and humic (sediment-rich) waters are particularly highly reflective in the red bands of visible light.

D.   THE COASTAL ENVIRONMENT

This section, provided only as supplemental information to optical water property studies, does not apply to data taken at Lake Tahoe, as it is an alpine lake with few of the dynamic processes seen in the ocean.   However, this section provides background information about some of the properties that must be considered when applying data analysis in the littoral regions of the oceans.

The coastal environment varies significantly from the open ocean in many ways. This is a region where hydrostatic conditions do not apply, where turbulent motions affect the entire water column, and where significant concentrations of biological constituents exist.

The Sea Star satellite's Sea-viewing WIde Field-of-view Sensor (SeaWIFS) is a 1.1 km spatial resolution multispectral sensor designed to distinguish between subtle color variations of the Earth's oceans. Algorithms are used to derive chlorophyll concentration and K_d at 490 nm, making this sensor a good resource for determining not only the optical properties of water, but also variations in chlorophyll concentration over the open ocean. SeaWIFS, using 6 visible and 2 near infrared (NIR) channels, is accurate over the open ocean, where the water is dark in the NIR channels. However, there are limitations to the SeaWIFs algorithm in coastal and inland waters as discussed in De Haan et al. (1997). These waters contain suspended sediments and macrophytes, each with their own spectral scattering and absorption properties

Sea grass. Plummer et al. (1997) performed an extensive sensitivity analysis on the effects of sea grass on the upwelling radiance of light. Five parameters were used: leaf-area index (LAI), turbidity, chlorophyll concentration, yellow matter concentration at nadir

(g440), and depth of water. LAI is directly proportional to the area of the sea grass leaves.

The results are shown below in Figure 2.3. The results show that subsurface reflectance from

sea grass depends most strongly on depth of the water, second on turbidity, and third on LAI.

Kruse et al. (1997) discuss analysis techniques of hyperspectral data for use in

studying coastal environments. Figure 2.4 shows the wide variations of reflectance spectra

found in coastal regions, collected from the Airborne Visible/InfraRed Imaging Spectrometer

(AVIRIS) hyperspectral sensor over Florida Bay.
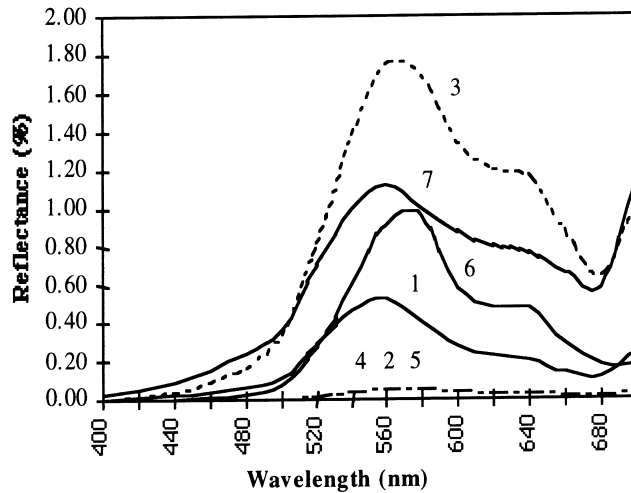
Scenario	LAI	Turbidity	Chlorophyll	G440	Depth
1	2.95	4.20	6.70	0.32	1.17
2	2.36	7.77	13.49	0.68	2.32
3	1.11	1.94	13.11	0.92	1.01
4	2.38	5.44	8.98	0.99	1.86
5	2.30	8.76	17.54	1.00	2.06
6	0.80	0.77	7.46	1.03	2.30
7	1.75	9.19	12.13	0.61	0.44

Figure 2.3. Figure 1 and Table 1 from Plummer et al. (1997), showing the effects of sea grass
on the reflectance of light.   Leaf Area Index (LAI), turbidity, chlorophyll, yellow matter at
nadir (g440), and depth all contribute to unique reflectance curves for each given scenario.

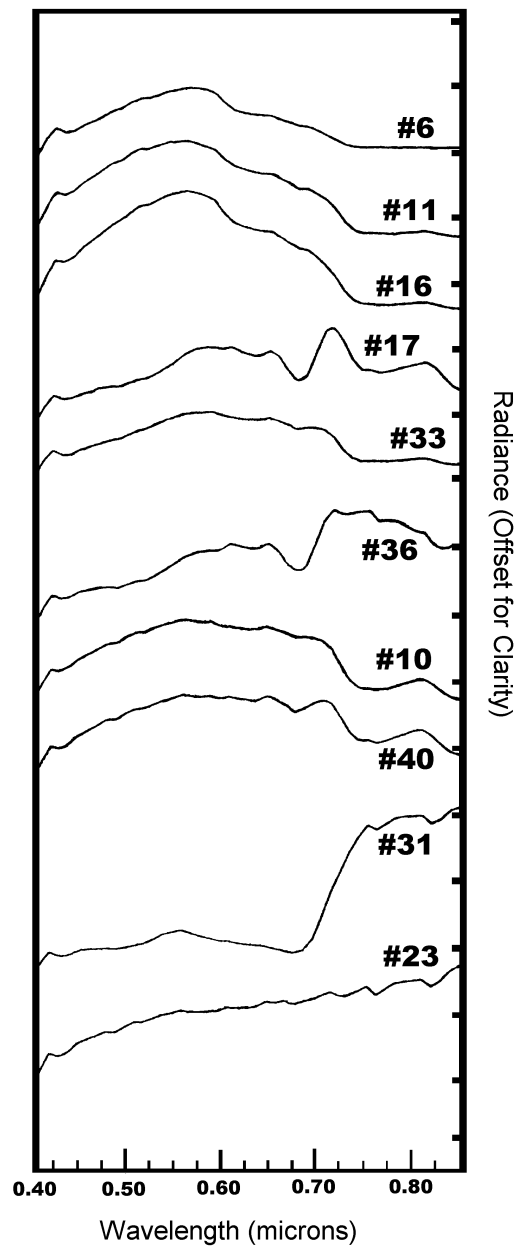| ID	Description
6	Blue-green algae 1
11	Blue-Green algae 2
16	Blue-green algae 3
17	Dense near-surface phytoplankton
33	Combination dilute phytoplankton/sea grass
36	Sea grass
10	Clear water over sediment 1
40	Clear water over sediment 2
31	On-shore vegetation
23	Sand/exposed sediment

Figure 2.4. Modified Table 2 and Figure 6 from Kruse et al. (1997), showing selected endmember spectra from AVIRIS data of Florida Bay. Notice the wide variation in water radiance values for different constituents.

12

E.   THE RADIATIVE TRANSFER EQUATION

A brief background on the Radiative Transfer Equation (RTE) as it applies to bathymetric work is presented. Mobley (1994) derives the radiance observed at a remote detector, L_d, for the case of an instrument viewing a water scene:

$$L_d = T_a \left[L_w + L_{ws} \right] + L_p,$$ (2.6)

where the symbols are defined in Figure 2.5. We are interested in L_w, the water leaving radiance term, also known as the volumetric contribution to L_d. as seen in figure 2.5, this term consists of contributions from both the bottom reflectance, A_d, and the water column itself, R_w.

Bierwirth et al. (1993) used a simplified form of the Radiative Transfer Equation (RTE) for the study of light emerging from a shallow body of water. When L_w is divided by the incident irradiance on the water surface, the irradiance reflectance just below the water surface is obtained:

$$R(0-) = \left(A_d - R_w \right) e^{-2K_d z} + R_w$$ (2.7)

Note how the first term decays exponentially with depth, implying that for deep water, only the water column itself will contribute to $R(0-)$. Another implication of this relation is that the bottom reflectance will play an important role in determining $R(0-)$.

To derive water depth z, Equation 2.7 is inverted and summed over n bands or wavelengths to solve for depth:

$$z = \sum_{I=1}^{n} \left\{ \frac{\ln \left(A_{dI} - R_{wI} \right) - \ln \left[R(0-)_I - R_{wI} \right]}{2nK_d} \right\}$$ (2.8)

13

In order to maintain a positive value for each logarithm in Equation (2.8), Stuffle et al. (1996) notes that over a dark bottom, the terms of each logarithm reverse, as R_w becomes the dominant term. Note that radiance terms must be converted to reflectance terms to use Equation 2.8.

Visible Light Path From Sun to AVIRIS Sensor

A_d Bottom irradiance reflectance

$R(0-)$ Irradiance reflectance just below the water surface

R_w Water column irradiance reflectance

L_{ws} Reflected radiance from water surface

E_0 Solar illumination at the top of the atmosphere

T_a Atmospheric transmittance

E_A Diffuse sky irradiance

L_p Atmospheric path radiance

L_T Target radiance transmitted by the atmosphere

L_d Radiance received at the sensor

E_d Downwelling irradiance

E_u Upwelling irradiance
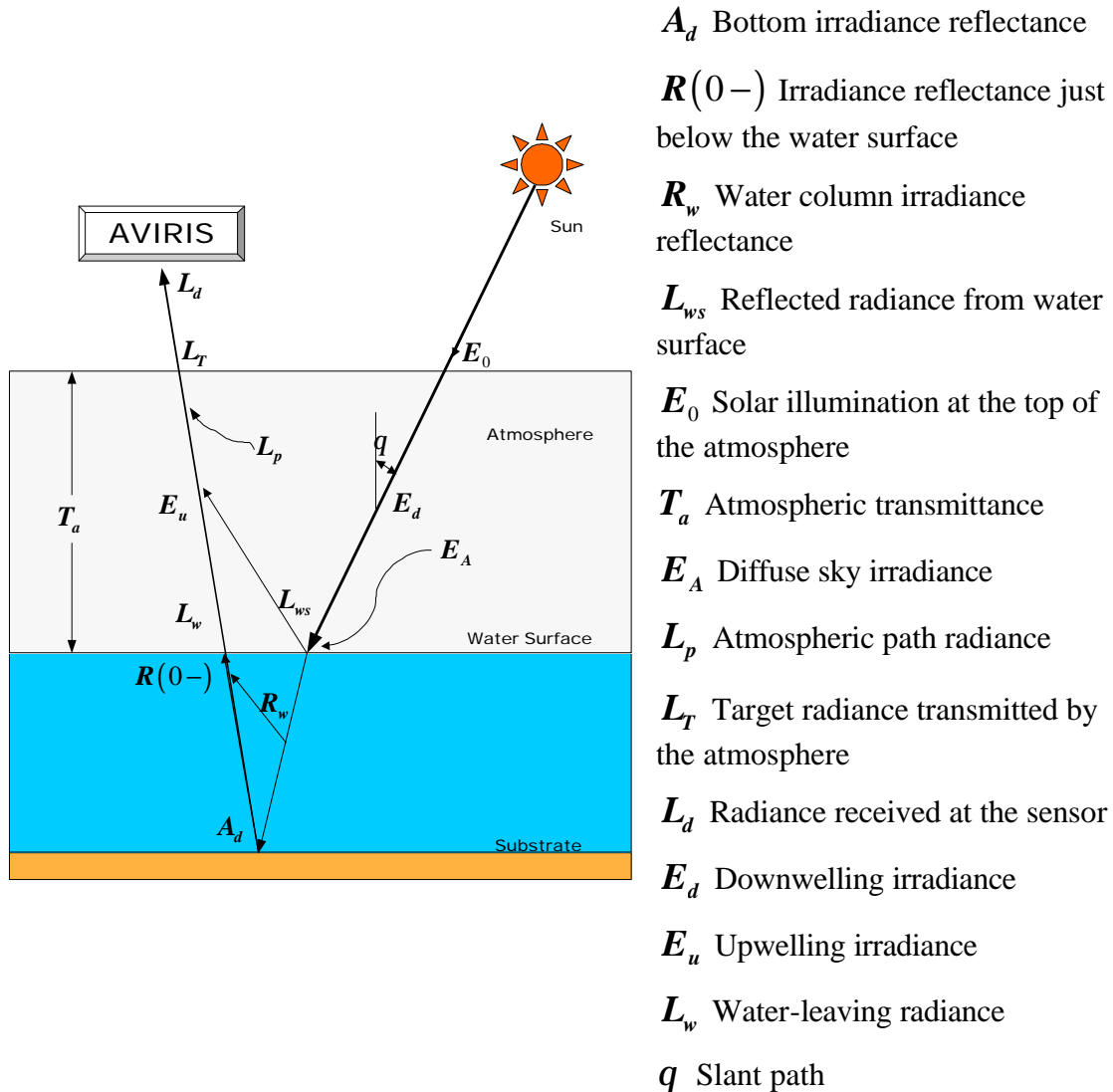
L_w Water-leaving radiance

q Slant path

Figure 2.5. Modified from Bierwirth et al. (1993) Figure 1, showing the multiple absorption and scattering paths that visible light undergoes before reaching the AVIRIS sensor.

THIS PAGE INTENTIONALLY LEFT BLANK

III.   DATA AND METHODS

A background on four topics of data collection and analysis will be discussed before proceeding to the actual data and methods. These topics include hyperspectral imaging and the AVIRIS sensor, principle component analysis, the MODTRAN atmospheric model, and the HYDROLIGHT water model. This will simplify our understanding of the steps that follow. The goal is to determine the values of the 4 variables, A_d, R_w, $R(0-)$, and K_d in Equation 2.8, applied to each pixel, thereby obtaining the depth at each pixel.

A.   TOOLS AND TECHNIQUES

1. The AVIRIS sensor

Imaging spectroscopy in general is the procedure of measuring the energy in numerous spatial resolution elements arriving at a sensor, and converting them to an image. By taking these measurements in very small bandwidths, say on the order of 10 nm, one can arrive at a nearly continuous spectrum for each pixel. If the pixels are small enough, they will essentially represent one element of an entire image or "scene". And, since each substance has a unique "fingerprint" or energy spectrum, one can theoretically determine which substances are in the scene based on the energy return at a sensor. Lewotsky (1994) presents an excellent history of imaging spectroscopy, and the evolution from multispectral imagers (with spectral resolutions of 100 to 200 nm) to hyperspectral imagers.

Hyperspectral imagers take advantage of narrow bandwidths ("hyper" meaning "many bands"). Stuffle et al. (1996) used the Hyperspectral Digital Imagery Collection

Experiment (HYDICE) sensor to study the Secret Harbor area on the eastern side of Lake Tahoe. On the same day that HYDICE data was taken, June 22, 1995, the AVIRIS sensor was flown over the same region of the lake. Johnson and Green (1995) describe AVIRIS as a nadir-viewing whiskbroom scanner containing 224 different detectors, each sensitive within a unique 10-nm bandwidth across the visible and near infrared (NIR) wavelengths of electromagnetic radiation, specifically 400 to 2450 nm. The AVIRIS takes an image with a swath of width 11 km, and typically 10-100 km long, partitioning the scene into pixels approximately 20 m by 20 m. AVIRIS is aggressively calibrated. In flight, this is done from a continuous spectral and radiometric reference. Twice per year AVIRIS is calibrated in the lab, where all aspects of AVIRIS data are compared to laboratory standards. Three times per year AVIRIS is calibrated in flight where performance is compared to theoretical predictions based on atmospheric measurements, surface reflectance measurements, and radiative transfer models.

2. Principle Component Analysis (PCA)

When looking at a hyperspectral image of an unfamiliar area, one needs to determine what components make up the scene, whether it be trees, rocks, water, etc. One technique of doing this is called Principle Components Analysis (PCA). Stefanou (1997) explains this procedure in detail. Essentially, a high correlation exists between adjacent bands in spectral imagery, and therefore a great deal of redundancy exists. PCA transforms these spectra to a new coordinate system, called N-dimensional or PC (Principle Component) space, so that the spectral variability is maximized. Mathematically, PCA diagonalizes the covariance matrix of the data by unitary transform, which identifies the combinations of

variables most responsible for the variances in the image. Then, the resulting eigenvectors are applied to each pixel vector, transforming it into a new vector with uncorrelated components ordered by variance. These eigenvectors act as weights to the original pixel brightness values. Applied to the 224 AVIRIS bands, a new image results associated with each eigenvector, called a principle component image or PC band. The set of PC bands are ordered from largest to smallest in terms of variance. For example, if a hyperspectral image is divided into ten PC bands, PC band 1 will contain most of the information about a scene, whereas PC band 10 will contain little. Throughout the remainder of this work, "real band" refers to one of the 224 AVIRIS bands, whereas "PC band" refers to the image after rotation into principle components.

3. Moderate Resolution Transmittance (MODTRAN)

The radiance received at the AVIRIS sensor is comprised of numerous components, including atmospheric scatter and upwelling surface irradiance. For the bathymetry problem, the atmospheric return components are considered as "noise", which must be "subtracted" out of the sensor-received radiance to reveal the water-leaving radiance. A model-based solution to this problem is to use a computer code called the MODerate Resolution TRANsmittance (MODTRAN) code. MODTRAN was developed by the Geophysics Division of the Air Force Phillips Laboratory; it calculates atmospheric transmittance and radiance from wavenumbers 0 to 50,000 cm^{-1}. The effects of absorption and scattering by molecules and aerosols are all integrated into this model. MODTRAN is operated using a number of input "cards" or lines of FORTRAN code, which the user must

modify to fit the problem. Nominally, card 1 is the atmospheric definition, card 2 the meteorological definition, card 3 the sensor placement, and card 4 the model resolution.

4. HYDROLIGHT

HYDROLIGHT, developed by Dr. Curtis D. Mobley, is a radiative transfer model that computes radiance distributions and derived quantities for natural waters, with the default model being salt water. Input to the model consists of the absorption and scattering properties of the water body, sea surface and bottom characteristics, and the sun and sky radiance incident on the sea surface. Output can be various irradiances, K-functions, and reflectances. Of importance to this work is obtaining a K_d index output. Mobley (1995) specifically notes that HYDROLIGHT is a radiative transfer model, and not a model of optical properties of water. Therefore, the user must supply the IOPs to the HYDROLIGHT code (HYDROLIGHT has a number of sub-models of water IOPs, though).

5. Summary

In summary, there are four steps to derive shallow water bathymetry using Equation 2.8. First, processing the AVIRIS hyperspectral data using the ENvironment for Visualizing Images (ENVI) software yields the bottom reflectance, A_d, one of the two volumetric components. Second, the HYDROLIGHT algorithm gives the diffuse attenuation coefficient, K_d. Third, MODTRAN solves for the various atmospheric components L_p, E_d, and T_a. These variables and Equations 2.3 and 2.6 will permit computation of $R(0-)$ directly; however, a different method for computation of $R(0-)$ will be used in this analysis.

Finally, a separate computer algorithm assimilates all of these variables and solves for depth based on the reflectances.

B.   THE SCENE

On June 22, 1995, the AVIRIS was flown on board an ER-2 aircraft at 2.35 km above Lake Tahoe, CA and NV, along the track shown in Figure 3.1. The instrument took data in 8 different scenes along that path. The resultant composite of three of these scenes is seen in the top portion of Figure 3.2. A portion of scenes 2 and 3 in the image were extracted to form a 531 by 614 pixel image that was analyzed. Of particular interest to this work is the region on the west side of the lake, bordering Tahoe City to Dollar Point, CA.
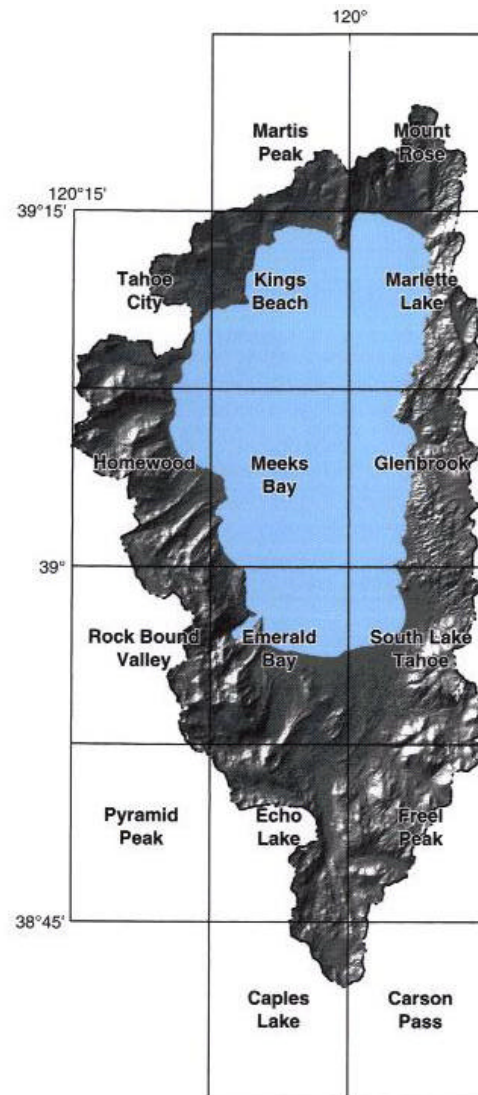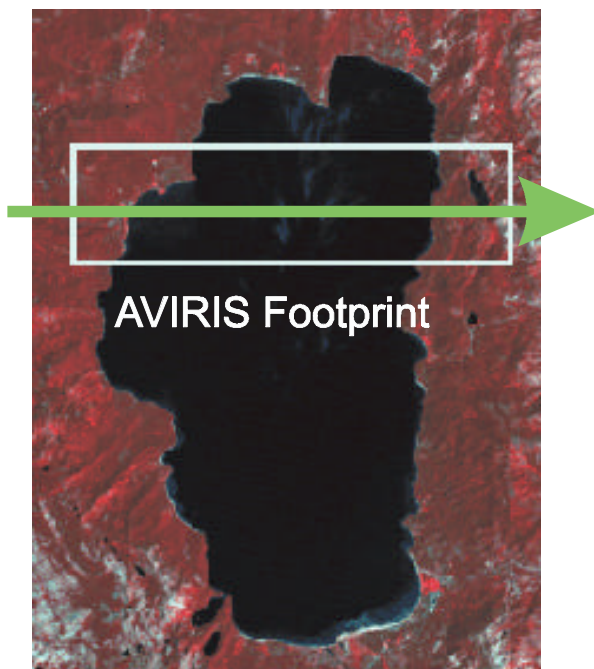
Lake Tahoe, Ca & NV

Figure 3.1. Lake Tahoe images from
http://tahoe.usgs.gov/Tahoe. The above
figure is derived from a USGS LANDSAT
image taken in 1990. The AVIRIS footprint
is shown in the white box for the June 22
1995 collect. The figure to the right shows
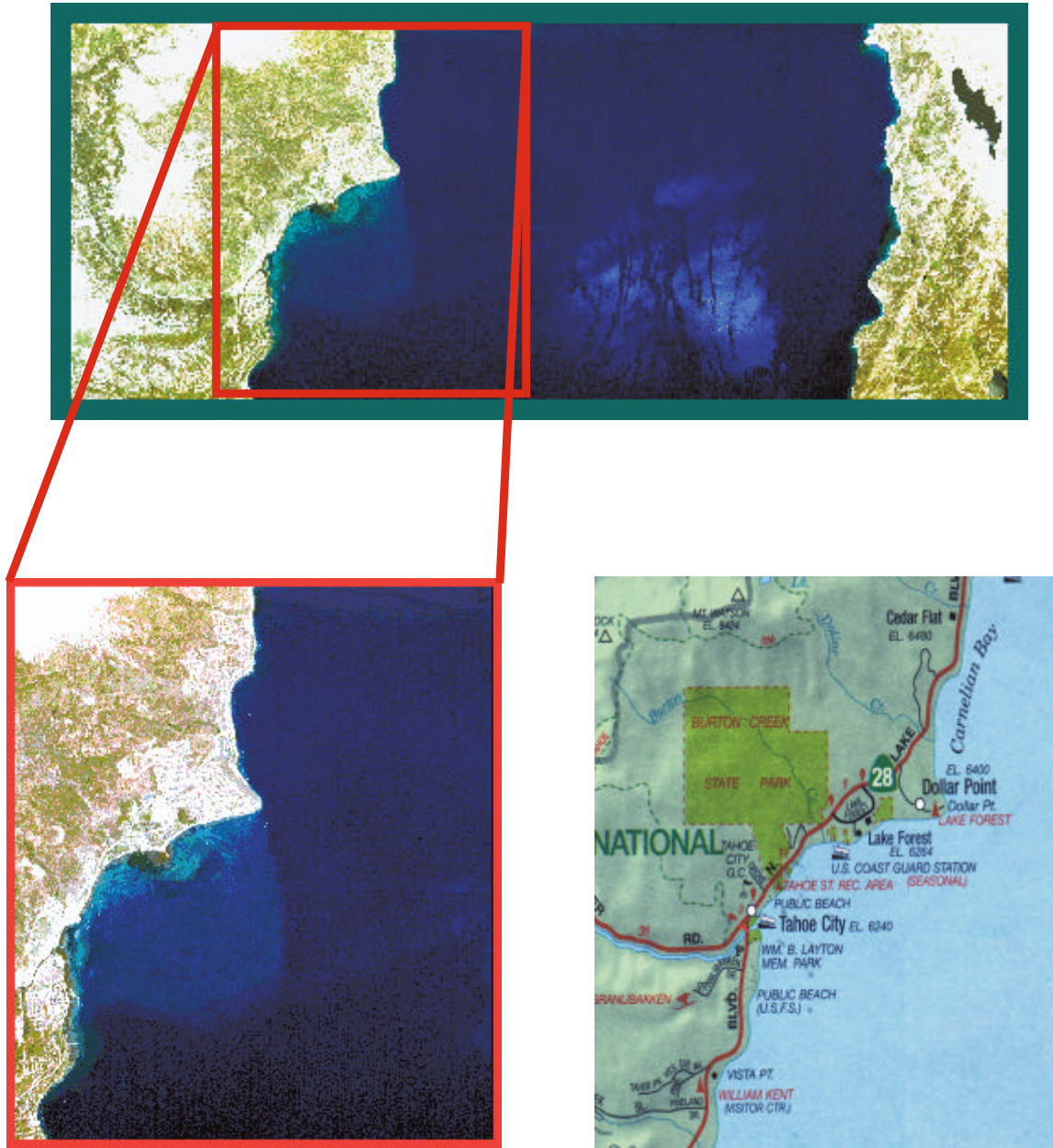the map coordinates

Figure 3.2. The top figure shows 3 frames of data from AVIRIS, created from the visible bands 28, 18, and 8, corresponding to 647.65 nm, 549.23 nm, and 451.22 nm, respectively. The dynamic range was scaled to allow details of the underwater structure to be revealed. Note the contamination of the data from the middle of the lake, apparently by a cloud reflecting off the water. Also, along the top edge of the image in the water is sunglint. The bottom figure on the left is the portion of the scene analyzed. On the bottom right is an Automobile Association of America (AAA) map showing the locations of nearby cities.

## C.   PROCESSING THE AVIRIS DATA TO SEGMENT THE SCENE

A first approach to the spectral data is to use principal components analysis to quickly distinguish the spectral regions, and determine the nature of any obvious sensor artifacts. Starting with a forward rotation, 10 PC bands were produced (see Figure 3.3). PCA was done here to determine spectrally unique regions of interest (ROI). The concept is that each
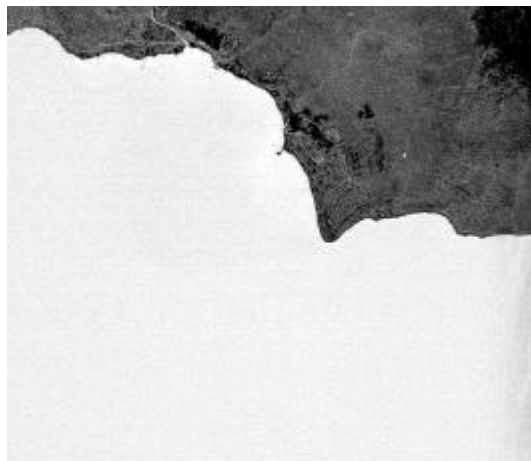

PC Band 1
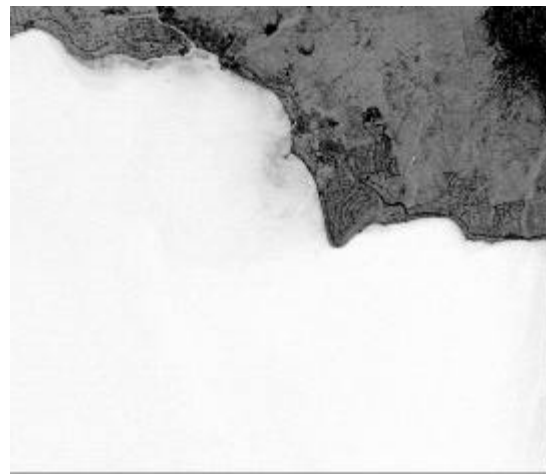
PC Band 2
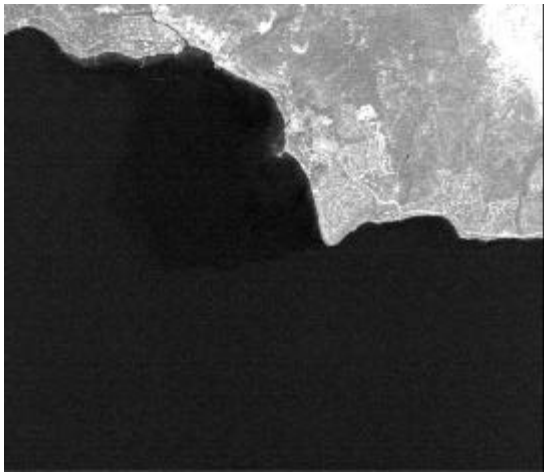
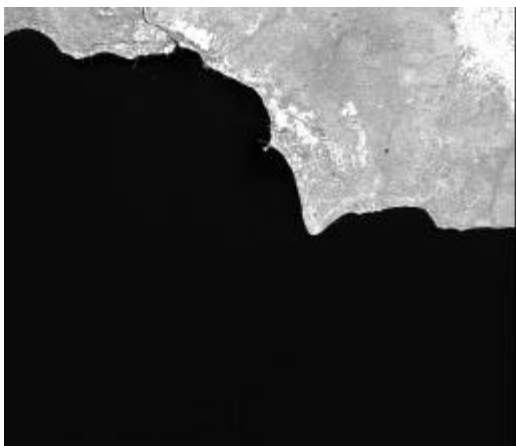PC Band 3

PC Band 4

Figure 3.3. PC Bands 1-4, rotated 90° clockwise.
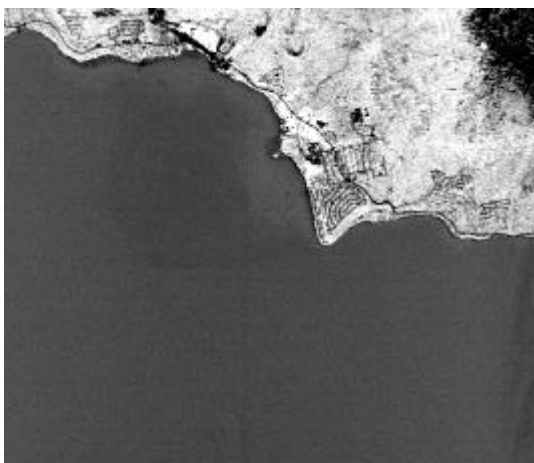
PC Band 5

PC Band 6

PC Band 7

PC Band 8

PC Band 9

PC Band 10

Figure 3.3 (continued). PC Bands 5-10.

ROI is spectrally unique due to one bottom type (or water type) throughout the region. For example, regions of distinct particulate or chlorophyll concentration should be separable. In this limited region, it appears that the water in the scene could be considered homogeneous in chlorophyll and particulate concentration throughout the region. Therefore, the PCA permitted isolation of unique bottom types and apparently a small oil slick. Then, based on visible images, such as that in Figure 3.2, PC band images (Figure 3.3), and/or a priori knowledge, a corresponding bottom substrate was inferred. With the distinct regions defined, it should be possible to use the "at-sensor" radiance, L_d, and perhaps a spectral library or database, applied to the ROI, to determine the bottom reflectance A_d for that region.

To segregate spectrally unique ROIs, first the 10 PC bands are input to an N-dimensional visualizer, where various combinations and numbers of PC bands are put into PC space and rotated in n dimensions. The extrema of the distributions, called endmembers, can be found in an iterative process. These are nominally the pixels with the purest spectral signatures. Pixels located in between two or three extrema are a linear combination of each extremum. In the work by Stuffle, this process could determine the pixels near the surface, that is, nearly pure "bottom" pixels, without a volumetric water element.

Figure 3.4(a) shows PC Band 1 with different ROIs highlighted in red. These regions were chosen from looking at both the "real" and PC Band imagery, and selecting interesting areas. Now, the red ROIs and corresponding portions of the 10 PC bands are then input to an N-dimensional visualizer, where various combinations of three PC bands are put into PC space and rotated in three dimensions. Figure 3.4(b) is a snapshot of a N-dimensional visualizer run using PC Bands 1, 3, and 5. In this snapshot, it is clear that three extrema

emerge, and hence three endmembers result. The extrema are colored as in Figure 3.5(a), and exported to the actual PC image, indicating different regions of interest (ROI). [See Figure 3.5(b).] Now a first guess on bottom type is made, based on the real band composite in Figure 3.2 and the PC Bands in Figure 3.3.
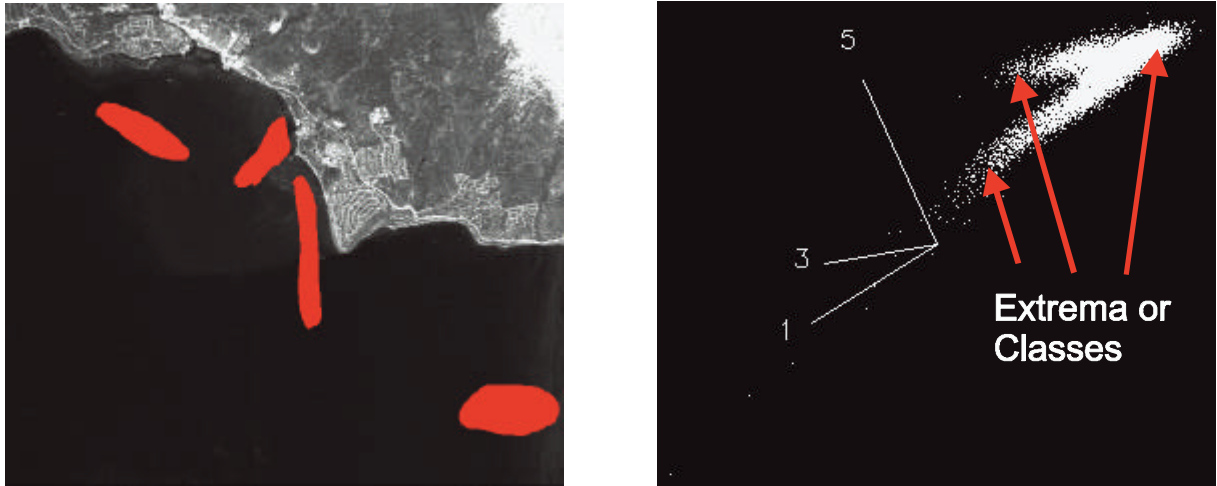

Figure 3.4. (a) PC band 1, showing the four ROIs chosen in the scene. (b) N-dimensional visualizer snapshot of the ROIs in (a) rotated in PC space using PC band 1, 3, and 5. Note the three distinct extrema on the scatter plot – these are the endmembers or classes.

The colors chartreuse, thistle, and coral appeared to be associated with shallow water, deep water, and sunglint, respectively. Now, Figure 3.5(a) is rotated again in PC space, using various combinations of three bands. When PC Bands 2, 3, and 9 are rotated, with the endmembers already defined from Figure 3.5(a), the snapshot in Figure 3.6(a) is obtained. One can still notice the small areas of the original endmembers.

Thistle comprises just a small piece of a unique cluster, and chartreuse is found throughout the upper portion of this highly linear scatter plot; those two areas are "filled" in

with their representative color, and the remainder is assigned to coral, the sunglint area, as

seen in Figure 3.6(b). In addition, Figure 3.7 shows the corresponding endmembers as they
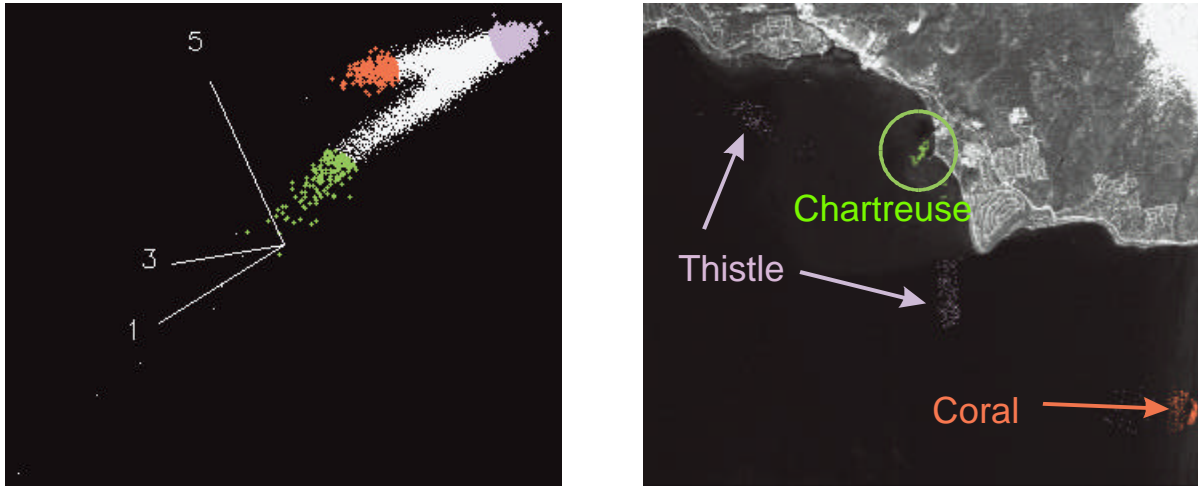
Figure 3.5 (a) (left) The three endmembers are colored chartreuse, coral, and thistle. (b) (right) The corresponding locations of the 3 endmembers from (a) transposed to PC Band 1. Based on the visual imagery, a first "guess" would be that coral corresponds to sunglint, chartreuse to shallower water areas, and thistle to deeper water areas.

Figure 3.6 (a) (left) Derived from taking Figure 3.5(a), changing to PC Bands 2, 3, and 9, and rotating to the given position. The thistle area is a small part of a much larger cluster. Coral is found within one narrow area, and chartreuse appears to dominate the upper portion of this linear scatter plot. (b) (right) The regions of (a) are "filled in" with their representative color.

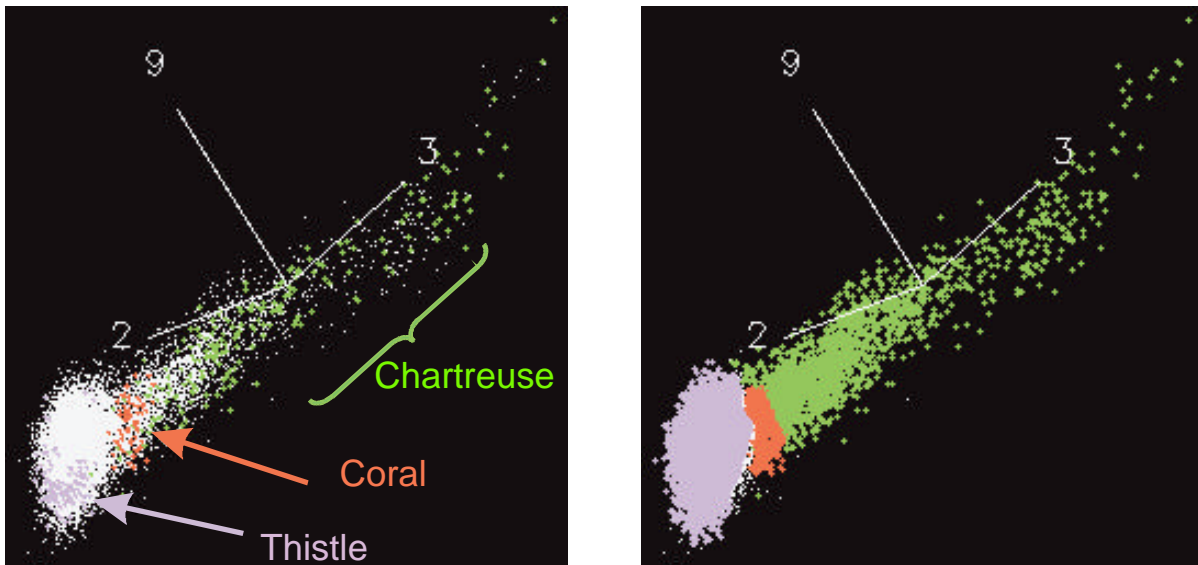make up the original ROIs, once exported back to the PC image in Figure 3.4(a). At this point, it is assumed that three main water types comprise most of the given ROIs. However, it was noticed that a variety of colors appear in the real band image of Figure 3.2. So, we
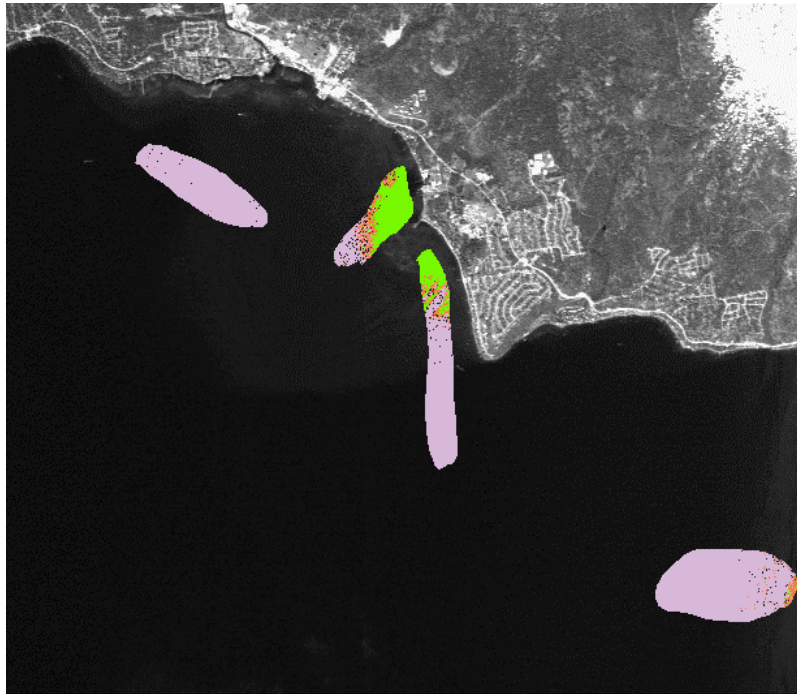
Figure 3.7. Figure 3.6(b) is transposed to the ROIs of Figure 3.4(a). Now, these original ROIs are divided into 3 basic water types, or classes.

came to the conclusion that the first "sum" of PCA classification on the shallower regions of water is not complete – a second iteration must be done to further isolate those smaller regions of spectrally unique water types. Since the thistle-colored points (deeper water) comprised most of the ROIs, it is desirable to look at the smaller endmembers (chartreuse and coral) to determine if more endmembers or structure in the scatter plots can be observed. This would lead to further subdivisions into new and different endmembers, and hence water types. So, the chartreuse (shallower water) was isolated and run though the N-dimensional visualizer, using PC Bands 2, 3, and 9, obtaining a scatter plot as seen in Figure 3.8(a).
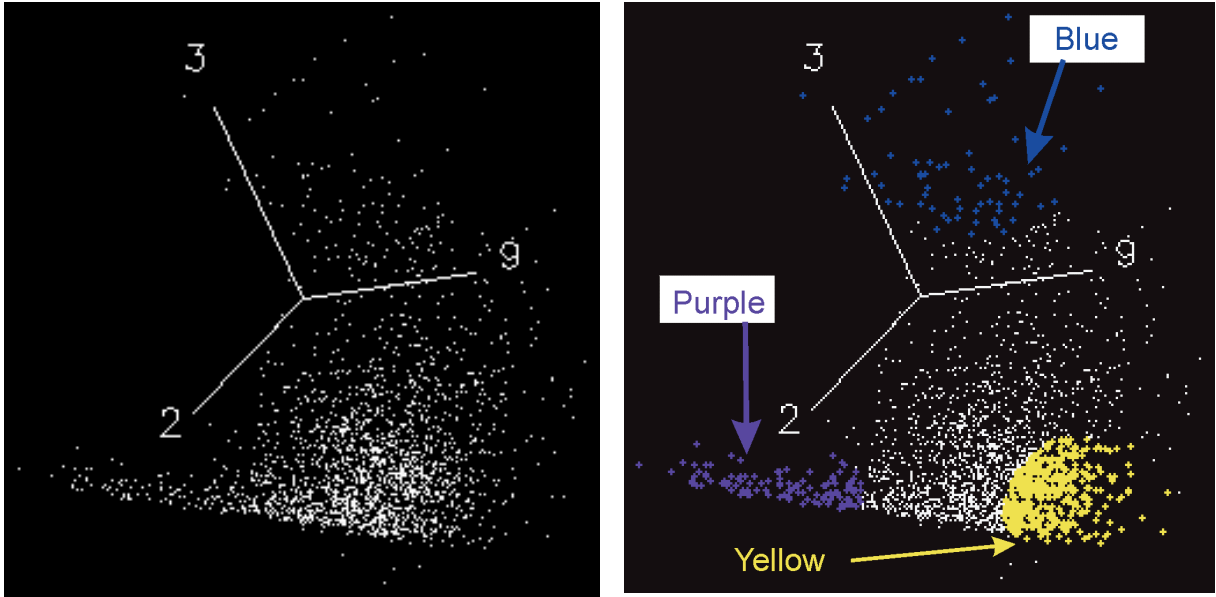
Figure 3.8 (a) (left) A scatterplot in PC space using just the chartreuse pixels from Figure 3.7, and using PC bands 2, 3, and 9. (b) (right) Three new endmembers emerge. All three new classes – blue, purple, and yellow - correspond to different areas of shallow water.

Figure 3.8(b) shows three distinct endmembers in this scatter plot. The 3 endmembers are transposed to PC Band 1 in Figure 3.9. Yellow appears to correspond to the rocky underwater areas and purple to part of the sunglint area and part of the graduation of depth from the rocky, yellow areas to a more sandy bottom. Blue corresponds to the area shown in a photograph (Figure 3.10) taken by the author on a recent visit there. This area contains sticks and tree limbs protruding from the water.

This process of subdivision of endmembers in the N-dimensional visualizer is continued, using various combinations of the PC Bands, until most of the ROI is covered by individual spectrally unique endmembers. Then other ROIs in the scene are created until all areas of interest from the Real Band images and the PC Band images are defined and spectrally unique.

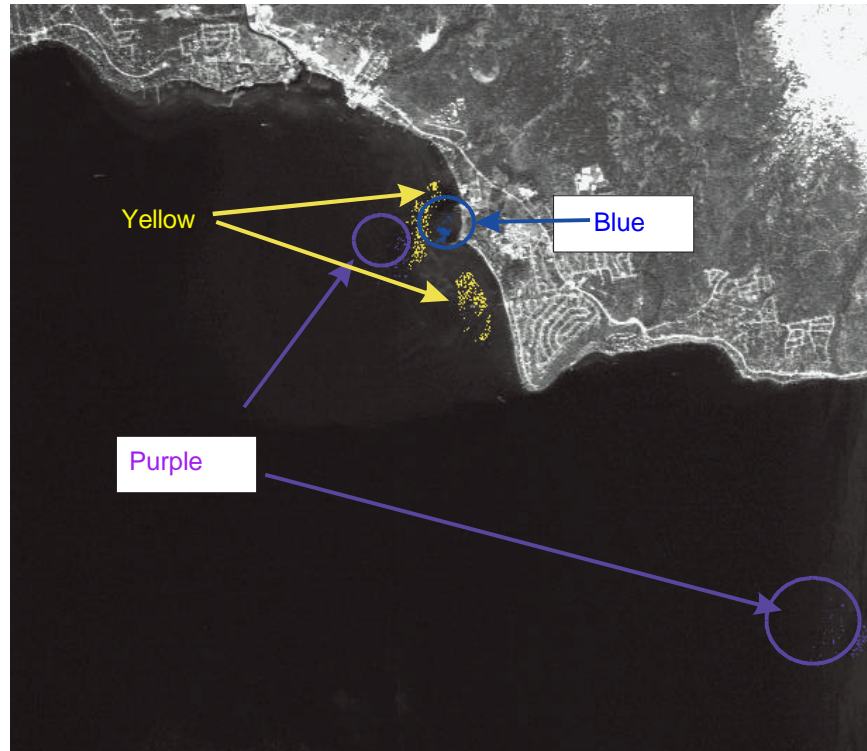Figure 3.9. Blue corresponds well the tree limbs in Figure 3.10. Yellow appears to be a very rocky bottom, as seen in Figure 3.2. Purple is a graduation of depth to a more sandy bottom mixed with sunglint areas.

Figure 3.10. A digital photograph of the blue ROI in Figure 3.9, taken by the author. The white box shows a region of protruding limbs and sticks.

Deep water and land are of no interest to this work, as the purpose is to obtain shallow water bathymetry. A land mask is created using Band 172 (1990.34 nm) to select the brightest pixels, and mask them from the image. Deep water, which is black in the IR, is selected in a similar manner and those data are masked. The shallow water region mean spectra are subsequently input into the ENVI maximum likelihood algorithm. The maximum likelihood algorithm statistically classifies pixels between distinct endmembers as one of those endmembers based on relative abundance of each endmember in that pixel. Figure 3.11 shows the resulting image after running the maximum likelihood classifier, and Figure 3.12 shows the mean spectra and given name for each endmember, or class. Note that the "oil slick" class was assigned to that region due to its spectral uniqueness and proximity to a
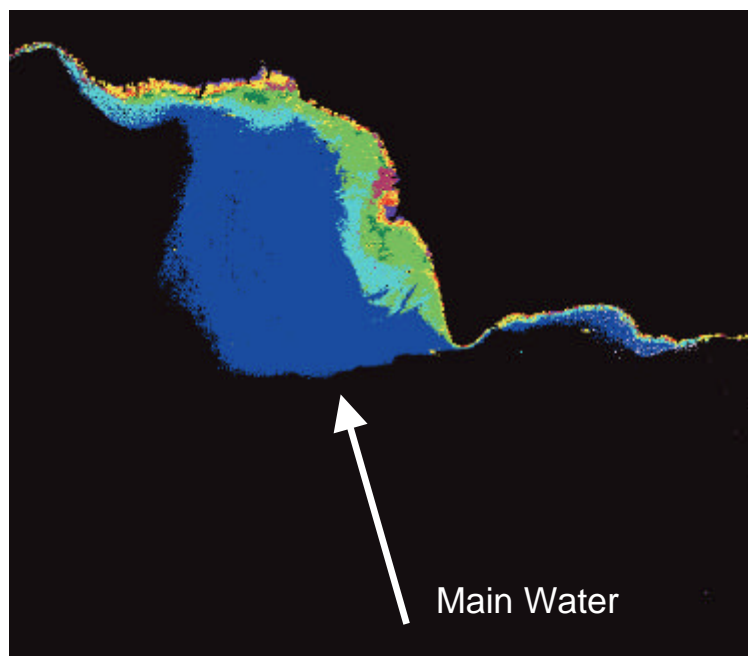

Figure 3.11. Spectrally unique classes of water. Mean spectra and class names are those given in Figure 3.12. Note that the land and deep water areas (black) are masked off.
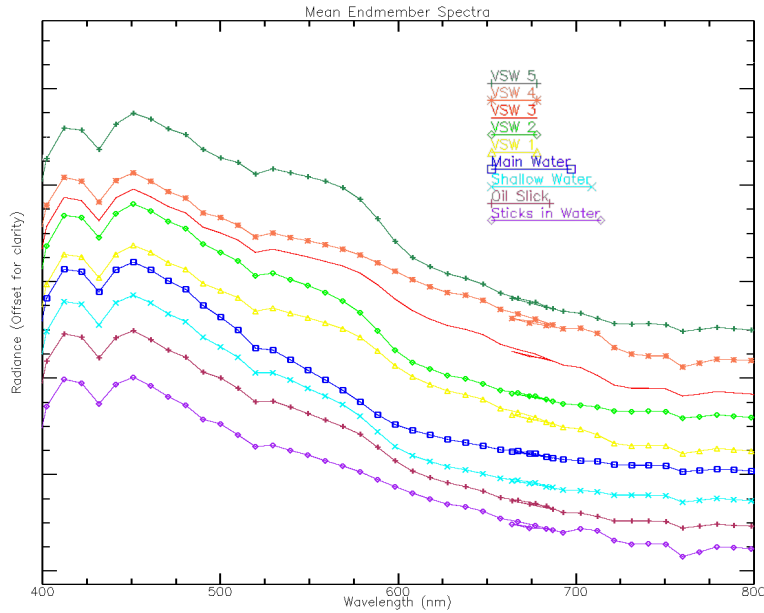
Figure 3.12. Plot of mean spectra of classes in Figure 3.11. Each spectrum is unique. Therefore, each will represent a different water column and/or bottom type. Note the overlap of data, between AVIRIS bands 32 (664.30 nm) and 33 (687.00 nm), caused by the overlap between AVIRIS spectrometers.

marina. "Sticks in water" refers to the aforementioned area in Figure 3.10. "VSW" refers to various regions of Very Shallow Water. Note that in Figure 3.12, a sensor artifact becomes apparent. The AVIRIS sensor uses four different spectrometers to cover the 400 to 2450 nm range. There is one spectrometer overlap that affects this work – that between AVIRIS bands 32 (664.30 nm) and 33 (687.00 nm). Therefore, in order to have continuous data to compare to HYDROLIGHT and to ultimately assimilate in the computer algorithm, AVIRIS bands 1-32 are kept.

At this stage, one would like to use the classified endmembers to determine the IOPs and bottom reflectance. Deep water could be used to determine IOPs (taking glint into account). Unfortunately, the AVIRIS spatial resolutions prevented exploiting the very shallow regions in the way Stuffle did. However, following in situ observations of Lake

33

Tahoe, the "Main Water" category of Figures 3.11 and 3.12 has a bottom composed of mostly sand and some rock. Stuffle et al. (1996) derived the bottom reflectance of wet sandy areas using the 210-band HYDICE sensor based on the water-leaving radiance of areas with very little water. This work first assumes that the bottom of this side of Lake Tahoe was made up of the identical type of sand, and used this same spectrum as an input for bottom reflectance. Figure 3.13 shows the reflectance spectrum used for wet sand, taken from Stuffle et al. (1996) HYDICE data. The HYDICE spectrum needed to be converted to match the AVIRIS spectral coverage. Note that in addition to instrumental (and atmospheric) differences, the HYDICE data were taken approximately 1 hour before the AVIRIS flight. Therefore, the errors in calculating reflectance for HYDICE will differ from the errors in the AVIRIS calculation.
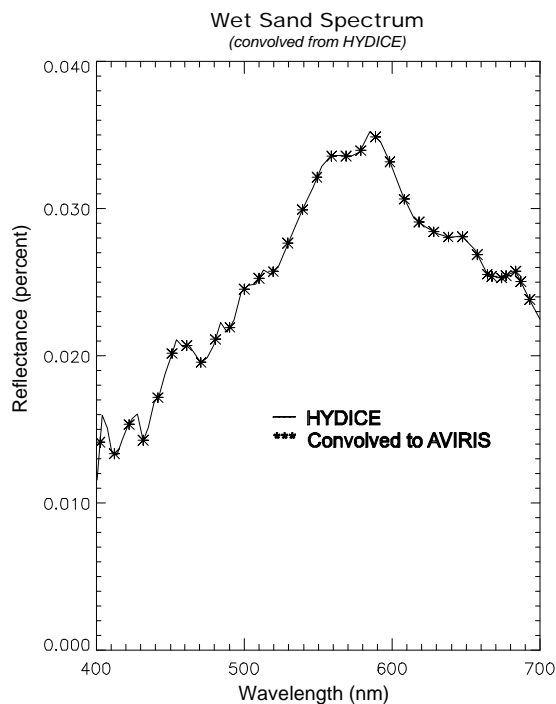

Figure 3.13. Bottom reflectance spectrum, taken from HYDICE and convolved to AVIRIS

Kappus et al. (1996) indicates that the chlorophyll content near the surface of Lake Tahoe is usually 0.2 mg/m^3. Therefore, the second assumption is made here that chlorophyll concentration is homogeneous throughout the water column, and has a value of 0.2 mg/m^3. The third assumption in this problem is that the water contains nil amounts of scattering particulates, as it is an alpine lake, and wind speeds have a negligible effect on disturbing the bottom.

Whereas Stuffle et al. (1996) showed 4 distinct ROIs, this much larger region of Lake Tahoe contains many more spectrally unique areas. Water constituents and bottom types, along with corresponding spectra of the other ROIs aside from "Main Water", were not available and could not be determined. As little is known about the other shallow regions in this ROI, the focus of this thesis became the "Main Water" region. So, now the bottom reflectance, A_d, in Equation 2.8, for the "Main Water" is known, or assumed for one area. This is where the depth calculation is performed. This leaves the diffuse attenuation coefficient, K_d, to be determined.

D.   USING HYDROLIGHT TO DERIVE K_d

HYROLIGHT was run assuming Type I infinitely deep water and calculating geometric depths. A separate FORTRAN subroutine that fixed the value of chlorophyll at 0.20 mg/m^3 was also used. Had chlorophyll values not been fixed, HYDROLIGHT would normally allow chlorophyll content to vary with depth. Table 3.1 shows the values input to the algorithm. Predefined AVIRIS wavelengths were input at which HYDROLIGHT would compute K_d, in order to match MODTRAN outputs.

HYDROLIGHT Parameter	Value
Phase Function	Pure Water (2)
Water Depth	Infinite
Bottom Reflectance	0.10
Output Depth Type	Geometric
Number of Depths (Depths Used)	8 (0, 0.01, 0.10, 0.11, 0.5, 0.51, 1.0, 1.01)
Julian Day	173
Latitude	39.14° N
Longitude	120.19° W
Time of Day	1900 Z
Compute Zenith Angle	Yes

Table 3.1. Input values to HYDROLIGHT. Output is K_d.

Once HYDROLIGHT was set to compute K_d values, the output in Figure 3.14 was produced. Note that K_d behaves as expected – as wavelengths become more red, more visible light is absorbed, resulting in a higher diffuse attenuation value.
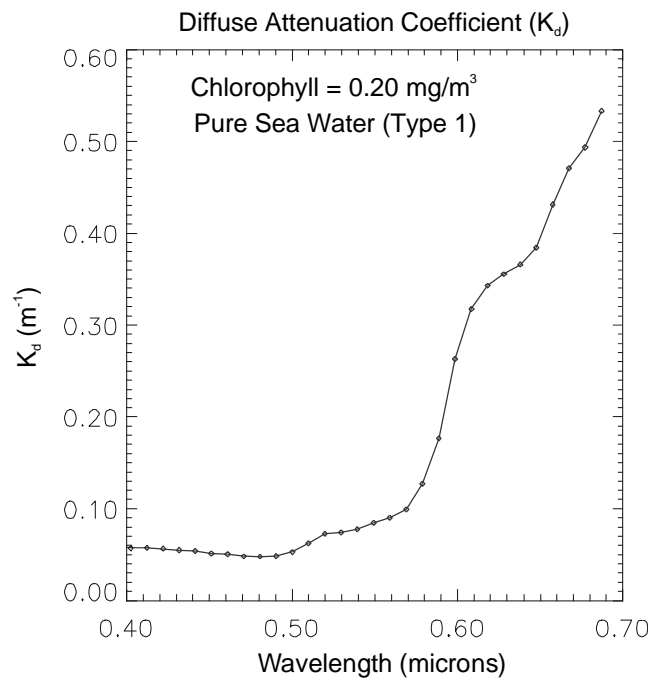

Figure 3.14. Diffuse attenuation coefficient, convolved to AVIRIS bands, using a constant chlorophyll value, assuming Type I water.

E.   ASSUMPTION ON WATER COLUMN IRRADIANCE REFLECTANCE

Finally, the variable R_w in Equations 2.7 and 2.8 must be accounted for. This is the portion of the volumetric contribution to L_w that comes from backscattered light from constituents in the water column. For the "Main Water" region of interest, based on a priori knowledge of the region itself, the assumption is made that the water column contains very few particulates that scatter light. Therefore, any attenuation of the visible light entering the water is due to a combination of chlorophyll and/or the water itself, i.e., absorbing materials. Therefore, $R_w \approx 0$. This assumption would not necessarily apply to the "VSW", "Sticks in Water", "Shallow Water", and "Oil Slick" areas of Figures 3.11 and 3.12; therefore $R_w \neq 0$ in these regions (more a priori knowledge of those areas would be needed). However, since the focus is on the "Main Water" ROI, for which we can assume, Equation 2.8 can be rewritten as:

$$z = \sum_{I=1}^{n} \left\{ \frac{\ln\left(A_{dI}\right) - \ln\left[R(0-)_{I}\right]}{2nK_d} \right\} = \sum_{I=1}^{n} \left[\frac{\ln\left(A_{dI}\right)}{2nK_d} \right] - \sum_{I=1}^{n} \left[\frac{\ln R(0-)_{I}}{2nK_d} \right] \quad ,$$

$$\text{where } \sum_{I=1}^{n} \left[\frac{\ln\left(A_{dI}\right)}{2nK_d} \right] = \text{constant} \qquad (3.1)$$

So, lastly, $R(0-)$ must be evaluated to solve Equation 3.1. The next section will show two different ways to do this – one using the aforementioned method of obtaining MODTRAN-produced values, and the other using the imagery itself to directly determine reflectance just below the water's surface.

F.   DETERMINING $R(0\text{-})$

Two methods are presented below to evaluate $R(0-)$, one using MODTRAN, coupled with Equations 2.3 and 2.6; and the other directly from the AVIRIS data itself, using brightness values.   The MODTRAN approach was not ultimately used for the depth calculation, but is shown below for completeness.

1. Using MODTRAN

MODTRAN was run to produce three important inputs to the depth calculation: L_p (path radiance) and T_a (atmospheric transmittance) from Equation 2.6; and E_d (downwelling irradiance) from Equation 2.3 that will permit determination of $R(0-)$ in Equation 2.7.   Note that for this calculation L_{ws} is assumed to equal zero, since the AVIRIS data was taken very close to noon local time, and the sensor was at nadir, minimizing direct reflectance off the water surface.   Table 3.2 shows the values input to MODTRAN for each of the two runs, one for L_p, and the other for E_d. T_a is a by-product of the first run. Of note is that when diffuse sky irradiance, E_A from Figure 2.5, was converted to sky radiance, the resulting values were two orders of magnitude smaller than L_p, and therefore disregarded in this calculation.

Since MODTRAN computes values at 1 nm separation, and AVIRIS bandwidths are ~9 nm, the MODTRAN data must be convolved to the corresponding AVIRIS bands, and hence lose resolution. Figure 3.15 shows a graphical representation of the 3 MODTRAN-

38

MODTRAN Parameter	Path Radiance	Downwelling Irradiance
Geographical/Seasonal Model	Midlatitude Summer	Midlatitude Summer
Atmospheric Path	Vertical/Slant	Vertical/Slant Path to Space
Scattering	Single	Multiple
CO_2 Mixing Ratio	360 ppmv	360 ppmv
Type of Extinction	Rural	Rural
Seasonal Aerosol Profile	Spring-Summer (2)	Spring-Summer (2)
Visibility	5 km	10 km
Altitude of Surface Relative to Sea Level	1.905 km	1.905 km
Initial Altitude	21 km	1.905 km
Final Altitude	1.905 km	100 km
Initial Zenith Angle	180°	20.6°
Julian Day	173	173
Scattering	Mie	Mie
Latitude	39° N	39° N
Longitude	120° W	120° W
Time of Day	1900 Z	1900 Z
Frequency Range	10000-25000 cm^{-1}	4000-25000 cm^{-1}
Frequency Increment	15 cm^{-1}	15 cm^{-1}

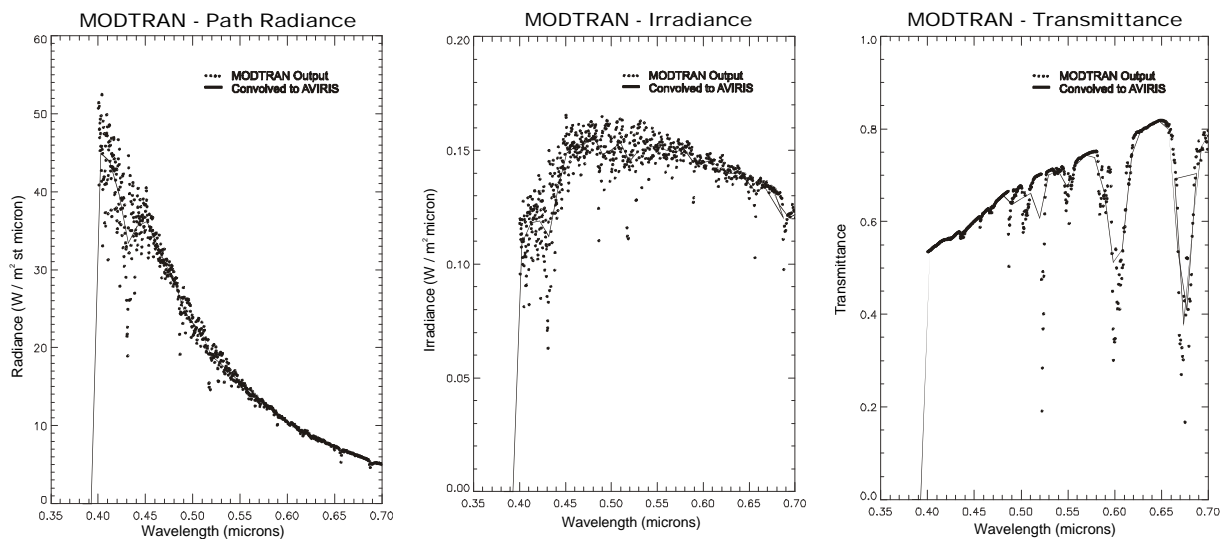Table 3.2. Input values to MODTRAN. Output was L_p, E_d, and T_a.

Figure 3.15. Graphical outputs of MODTRAN for L_p, E_d, and T_a.

produced variables needed. The dots are the MODTRAN output, while the line plot represents the MODTRAN output convolved to AVIRIS bands. Note the spectrometer overlap artifact between 650 and 700 nm.

Finally, all three of these variables may be compiled in the final algorithm to determine depth. This somewhat tedious approach depends on a number of assumptions about the atmospheric conditions, and did not seem well suited to the data at hand (many dark pixels), resulting in negative values for reflectance. A more appropriate way of extracting the reflectance just below the water surface is presented next.

2. Converting AVIRIS radiance data to reflectance – flat fielding[*]

The first 40 AVIRIS bands are input to an algorithm that extracts the brightest 0.5% and the darkest 0.5% pixels from each of the 40 bands, with the darkest pixels taken to be over ground locations of zero reflectance. Hence, these pixels give the sky radiance (no other contributions to L_d). Figure 3.16 shows the extrema of pixel brightness. In this manner, a "scale" of reflectance is created. The algorithm consists of taking the darkest pixels from each band and assigning a reflectance of zero to them; and the brightest pixels are assigned a value of one. Then, the radiance of the darkest pixel is subtracted from every pixel in the image, acting to "re-scale" the image. Finally, all pixels in the image are "normalized" by the difference between the brightest and darkest pixels, and multiplied by 100; now, the scene is in reflectance space. Algebraically:

---

[*] The ENVI tutorial illustrates the widely varying results one can obtain in a radiance-to-reflectance calculation with different techniques.
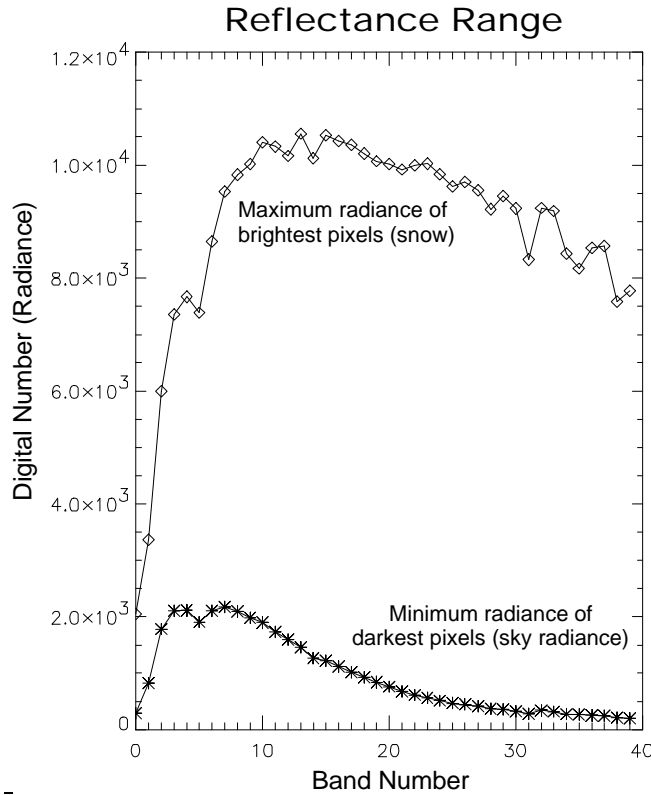
Reflectance Range

Figure 3.16. Minimum and maximum reflectances of the 99th percentile of the brightest and darkest first 40 AVIRIS bands. Every remaining reflectance value falls in between.

$$\frac{(AVIRIS\ radiance\ value - sky\ radiance\ value) \times 100}{(Brightest\ radiance\ value - sky\ radiance\ value)} \quad\quad (3.2)$$

Briefly, MODTRAN and flat fielding are compared. Figure 3.17(a) shows the comparison of the minimum path radiances, while Figure 3.17(b) shows the ranges of radiance values for each method. It appears that MODTRAN, as run above, has produced radiances that are too large. Figure 3.17(b) differences are primarily due to the AVIRIS bandwidths.

Figure 3.18 is a histogram of the total number of occurrences of varying reflectances from 0 to greater than 100. To note, the brightest pixels in each scene were those covering the area of snow to the northwest of Tahoe City (white patches in Figure 3.2). The

41
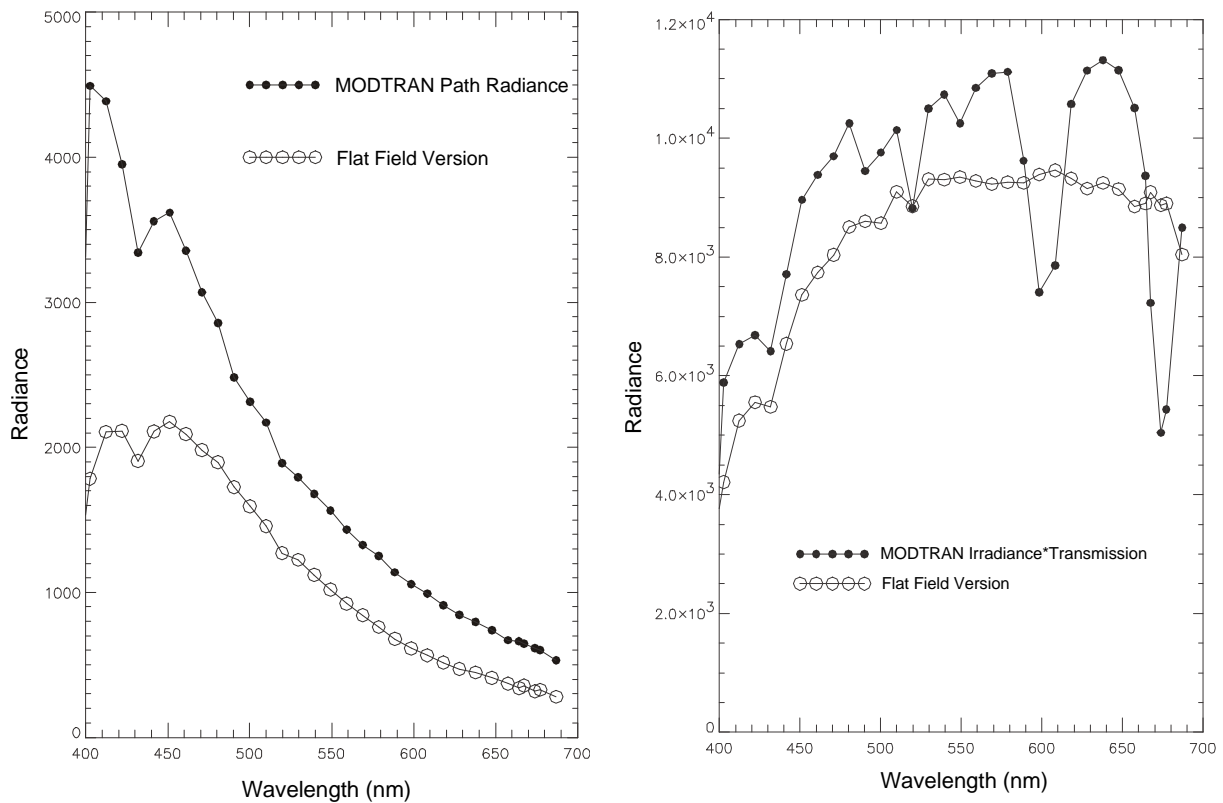
Figure 3.17. Comparison of flat field results to MODTRAN calculations. a) (left) Minimum radiance compared to MODTRAN path radiance. b) (right) Flat field max-min compared to MODTRAN irradiance*transmission.

darkest pixels varied - in the first 5 bands, they tended to be the "Oil Slick" regions of Figures 3.11 and 3.12; and in the higher bands, they tended to be areas of the water. Note that this approach allows reflectance to exceed 100%, but for a very small number of pixels.

Now, to explore the new reflectance space data, a PCA was done on the newly created reflectance bands, in order to look at the deep and shallow water areas. Figure 3.19(a) is PC Band 2 in reflectance space with 2 different ROIs – a part of the Main Water region we are interested in computing depth for, and parts of the deeper water – along with their mean spectra. Note that these spectra are computed in reflectance space and are

Brightness Values for AVIRIS Bands 1-40
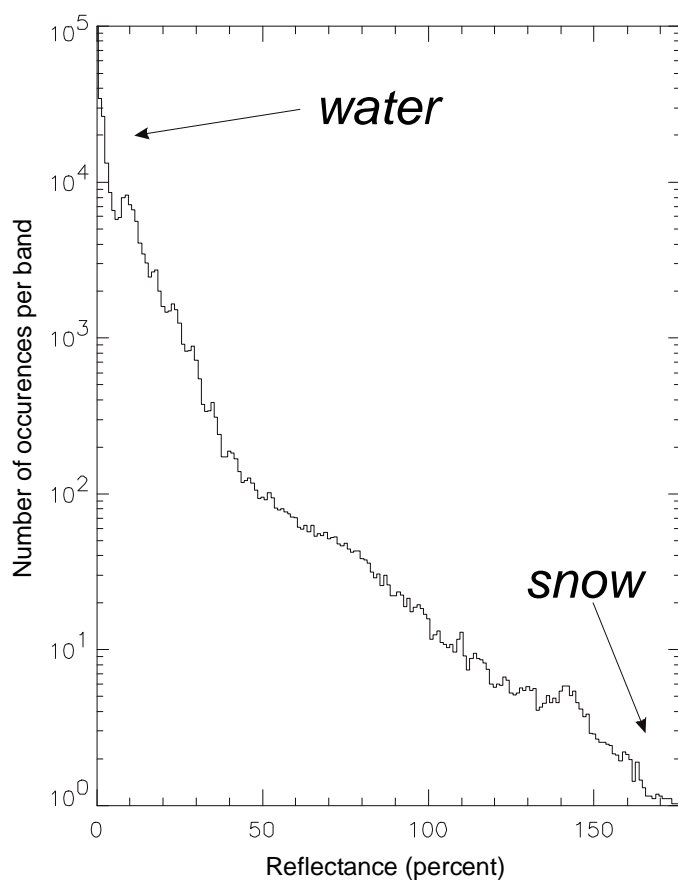
Figure 3.18. Histogram showing the distribution of reflectance values for the scene. Note that darkest pixels tend to be deep water, and brightest are snow cover on land.

therefore unrelated to the spectra computed in radiance space in Figure 3.12. Note the region of separation between the mean spectra for both ROIs in Figure 3.19(b). This separation in spectra is due to the bottom reflectance contribution of the Main Water region. Also, note that below 420 nm, an obvious sensor artifact exists, creating bogus data. Above 600 nm, there is no bottom reflectance component emerging from the data. Therefore, it was concluded that the only good data to use for the depth calculation was between 420 and 600 nm, which corresponds to AVIRIS bands 5 to 24.
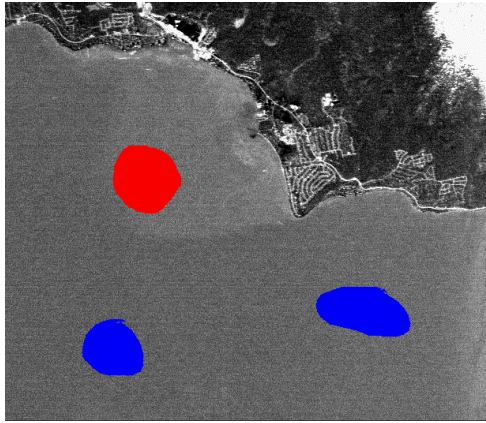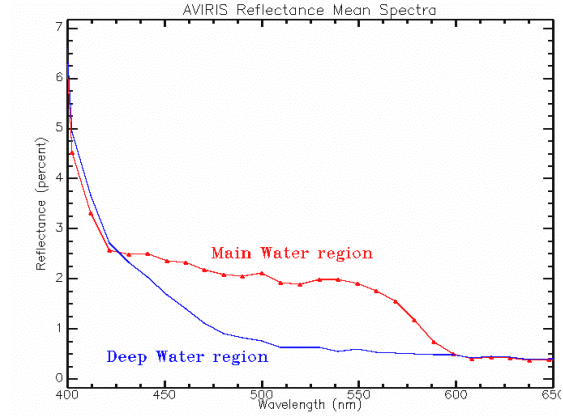
(a)   (b)

Figure 3.19. (a) New ROIs in PC reflectance space band 2, chosen over the Main Water region from Figure 3.14 and deeper water. (b) Mean spectra of the two ROIs in (a). Note the separation between them, mainly due to the bottom reflectance. Below 420 nm a sensor artifact is apparent.

G.   ASSIMILATING DATA TO DERIVE DEPTH

Now, based on Equation 3.1, a computer algorithm was devised that assimilated the three variables, A_d, K_d, and $R(0-)$, and applied to AVIRIS bands 5 to 24. The major elements of the equation are shown in Table 3.3. The data outputs and results are discussed in Chapter IV.

As a practical matter, since there is only one bottom type assumed, Equation 3.1 shows that we can ignore the bottom reflectance for the given calculation. The bottom reflectance term, summed for the spectrum shown in Figure 3.13, gave an offset of 5.9 m. After much effort, all that was needed was remote sensing reflectance and K_d.

44

Computer Algorithm to Derive Water Depth

Input AVIRIS reflectance data

Input bottom reflectance (wet sand spectrum for this case) from spectral library

Input HYDROLIGHT-generated diffuse attenuation coefficient

Apply Equation 3.1 over AVIRIS bands 5-24

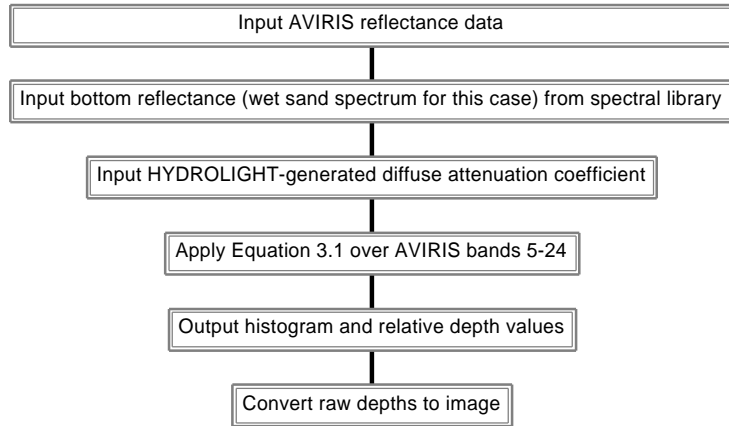| Output histogram and relative depth values |
|---|

Convert raw depths to image

Table 3.3. The major steps of the computer algorithm that reveals water depth.

THIS PAGE INTENTIONALLY LEFT BLANK

IV. RESULTS AND DISCUSSION

Of note, the computer algorithm was applied to the entire region in Figure 3.11, with only land masked out. This was done for illustrative purposes only – the results in the Main Water region are the only portion expected to be accurate.

A. COMPARISON OF RESULTS TO USGS BATHYMETRIC CHART

Upon executing the computer algorithm, a histogram was first produced to indicate the relative depth (with respect to some fixed point) of all the pixels. Figure 4.1 shows interesting implications of the data. Note the range and distribution of all pixel values. The range is from approximately –20 to 5 m. The Main Water region shows its own specific Gaussian distribution near the shallow region of the histogram, while a large distribution of the deep water pixels, sunglint, and sensor artifacts make up the majority of the pixels. Again, the only region for which the calculation would be expected to be accurate is the Main Water region depicted in Figure 3.11 – the calculated values in the remaining regions are shown only for completeness.

Since 5 m was the highest point in the relative depth range (with land areas having been masked out), it was assumed that the highest point in the remaining water scenes is zero. So, 5 m was subtracted from all values, producing the depth image shown in Figure 4.2.

Figure 4.3 is the United States Geological Survey (USGS) bathymetric chart corresponding to the Main Water and VSW areas of Figure 3.11. Figure 4.2 was cropped to approximately the same area as the one shown in Figure 4.3, and the result is given in Figure 4.4.
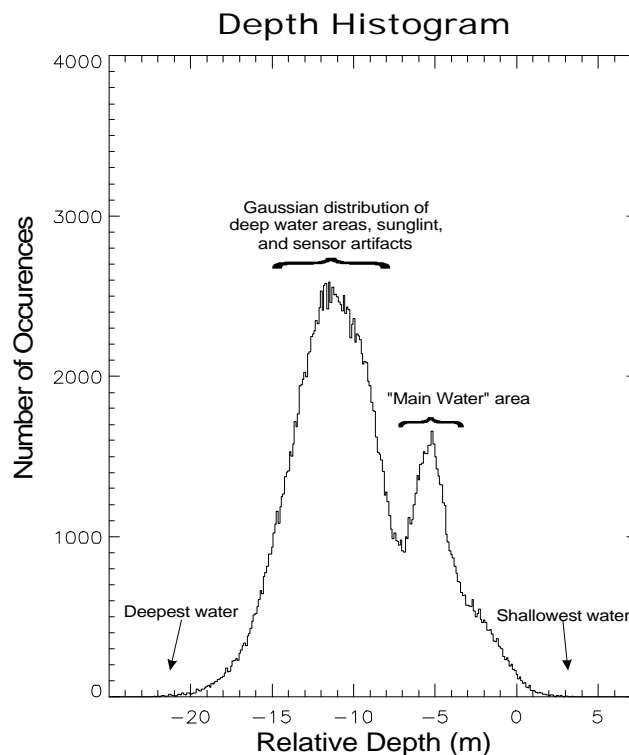
Figure 4.1. Depth histogram showing the depth calculation algorithm results as it applies to all ROIs in Figure 3.11, including deep water areas (but not land).

Comparing Figures 4.3 and 4.4, the "Main Water" region in the USGS chart (converted to meters) varies from 10 to 15 m. The spectral algorithm output varies from 7 to 11 m in this same region: the algorithm produced values are offset from those on the published USGS chart, but show a similar range of variation[*]. Comparing Figures 4.2 and 4.3, values are off as expected, greatly in the "Sticks in water" and "Oil slick" regions. This is due to the fact that the water column itself is not homogeneous, in addition to differences in bottom type. Major differences should ultimately be due to two factors:

---

[*] There are some indications that the range of depths produced by the algorithm is some 30-50% less than the actual range in the "Main Water" region.

AVIRIS Derived Depth Chart — Lake Tahoe
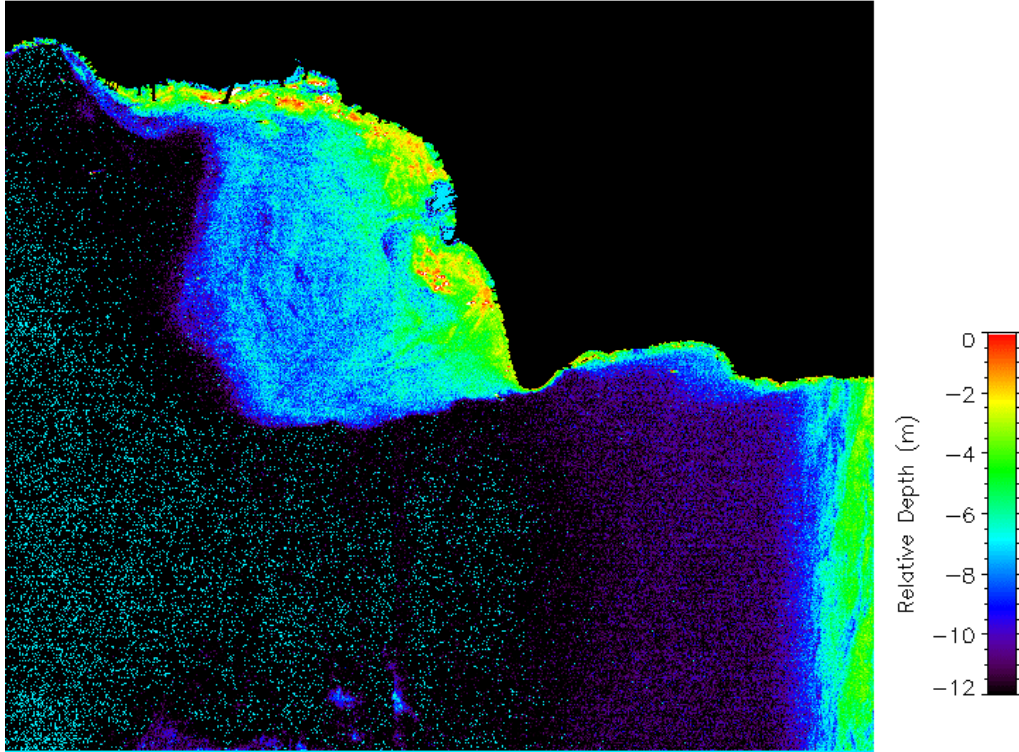
Figure 4.2. The algorithm outputs for depth. Note, for this scene, deep water and sunglint are not masked out as they were in Figure 3.11. Also, the Main Water region from Figure 3.11 is the only region that is expected to have reasonably accurate results.

- errors in K_d will introduce an overall proportionality (Equation 2.8), and

- errors in bottom reflectance will produce an overall offset.

B.   SOURCES OF ERROR AND LIMITATIONS

Possible sources of error. There are many possible sources of error to this calculation. Aside from geographical coordinate and coastline misalignment, most were likely from assumptions that went into this problem. Notably, the assumption that the entire water column under each pixel was homogeneous and contains nil scattering constituents $(R_w = 0)$

may not be accurate. Choosing a constant value for chlorophyll implies that organisms are found uniformly throughout the water column, which is not true. Also, the default HYDROLIGHT model used is intended for use in salt water, not fresh water.

Figure 4.3. USGS (January, 1987) bathymetric chart for the Main Water and VSW areas of Figure 3.11. Soundings are in feet.
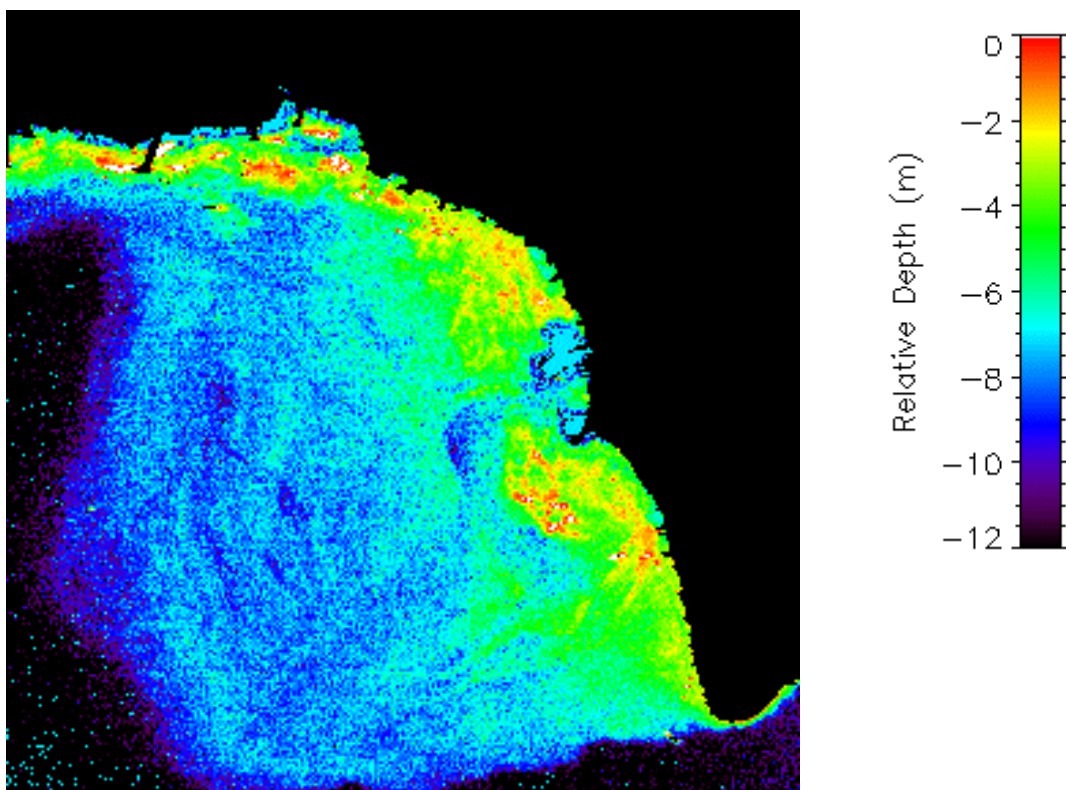
Figure 4.4. Portion of Figure 4.2 corresponding to the USGS chart in Figure 4.3. Depth scale is in meters.

Limitations. Perhaps the biggest limitation of using this method is the under-determined nature of the problem and the two necessary ingredients to solve it – the bottom type and chlorophyll/particulate concentration. A priori knowledge of the bottomtype, and acquisition of the corresponding bottom reflectance spectrum from a spectral library, is the preferred method for obtaining bottom reflectance for use in the computer algorithm. However, through tedious data analysis, it is possible to extract a good estimate of the bottom material with a higher spatial resolution sensor (Stuffle et al. 1996).

As far as chlorophyll/particulate concentration, the variability throughout the water column should be known, especially for the more turbulent and euphotic coastal regions

where it can vary dramatically over depth. In these cases, R_w will make a significant contribution to L_d and cannot be discounted.

The other important limitation, mostly due to the determination of bottom type, is the cumbersome "finessing" of the data that must be done to input into the computer algorithm. The ideal scenario would be one where this process is automated, but convolving of the MODTRAN and HYDROLIGHT outputs to fit the AVIRIS sensor channels, along with conversion of AVIRIS radiance data to reflectance data (and the many possible methods to do this), makes this algorithm unique for AVIRIS only (not HYDICE or the other types of hyperspectral sensors) and in itself generates errors.

C.   FUTURE RESEARCH

One possible area for future research would be the application of the computer algorithm to the littoral areas of the world, starting with a simpler region (such as clear tropical waters devoid of heavy chlorophyll) and working toward more turbulent and euphotic coastal zones.

Another endeavor would be the comparison of this method to that of the LANDSAT algorithm. LANDSAT data can be used in a similar method to compute water depth using Band 2 (green) and interpolating values of brightness to water depth.

Again, the most tedious part of this work was identifying bottom types. But, the U. S. Navy has a potential solution on the way – the Hyperspectral Remote Sensing Technology (HRST) program. Wilson and Davis (1998) describe HRST as the program where the Naval EarthMap Observer (NEMO) satellite, due to launch in mid-2000, will carry the 210-channel

Coastal Imaging Spectrometer (COIS) to provide images of littoral regions of the world. Then, the Optical Real-time Adaptive Spectral Identification System (ORASIS) will crop these images to a more manageable size, and will compare the spectra in the scene to a database corresponding to physical objects. The spectra will be "unmixed", and the scene elements derived. With a resolution down to 5 m, this database will have huge implications for many areas of research, including the important input for bottom reflectance into the bathymetry problem. A final area of research would be the comparison of HRST bottom types to those found through PCA analysis, once these data become available.

THIS PAGE INTENTIONALLY LEFT BLANK

LIST OF REFERENCES

Bierwirth, P. N., Lee, T. J., and Burne, R. V., "Shallow Sea-Floor Reflectance and Water Depth Derived by Unmixing Multispectral Imagery," *Photogrammetric Engineering and Remote Sensing*, Vol. 59, No. 3, March 1993, pp. 331-338.

De Haan, J. F., Kokke, J. M. M., Hoogenboom, H. J., and Dekker, A. G., "An Integrated Toolbox for Processing and Analysis of Remote Sensing Data of Inland and Coastal Waters – Atmospheric Correction," paper presented at the Fourth International Conference on Remote Sensing for Marine and Coastal Environments, Orlando, Florida, 17-19 March 1997.

Dekker, A. G., Hoogenboom, H. J., Rijkeboer, M., de Haan, J. F., and Buiteveld, H., "Estimation of Water Quality Parameters of Inland and Coastal Waters With the Use of a Toolkit For Processing of Remote Sensing Data," paper presented at the Fourth International Conference on Remote Sensing for Marine and Coastal Environments, Orlando, Florida, 17-19 March 1997.

Jerlov, N. G., *Marine Optics*, Elsevier, Amsterdam, 1978.

Johnson, H. K. and Green, R. O., "Summaries of the Fifth Annual JPL Airborne Earth Science Workshop: Volume 1. AVIRIS Workshop," JPL Publication 95-1, Vol. 1, pp. 105-108, 1995.

Kappus, M. E., Davis, C. O., and Rhea, W. J., "HYDICE data from Lake Tahoe: Comparison to coincident AVIRIS and in-situ measurements," Proceedings of the SPIE, Volume 2819, Denver, Colorado, August 1996.

Kruse, F. A., Richardson, L. L., and Ambrosia, V. G., "Techniques Developed for Geologic Analysis of Hyperspectral Data Applied to Near-Shore Hyperspectral Ocean Data," paper presented at the Fourth International Conference on Remote Sensing for Marine and Coastal Environments, Orlando, Florida, 17-19 March 1997.

Lewotsky, K., "Hyperspectral Imaging: Evolution of Imaging Spectroscopy," OE Reports, November, 1994.

Mobley, C. D., Light and Water: Radiative Transfer in Natural Waters, Academic Press, 1994.

Mobley, C. D., *HYDROLIGHT 3.1 Users' Guide*, SRI International, Menlo Park, California, 1995.

Plummer, S. E., Malthus, T. J., and Clark, C. D., "Adaptation of a Canopy Reflectance Model for Sub-Aqueous Vegetation: Definition and Sensitivity Analysis," paper presented at

the Fourth International Conference on Remote Sensing for Marine and Coastal Environments, Orlando, Florida, 17-19 March 1997.

Smith, R. C., and Baker, K., "The Bio-optical State of Ocean Waters and Remote Sensing," *Limnology and Oceanography*, **23**(2), 247, 1978.

Stefanou, M. S., Olsen, R. C., and Cristi, R., *A Signal Processing Perspective of Hyperspectral Imagery Analysis Techniques*, Master's Thesis, Naval Postgraduate School, Monterey, California, June 1997.

Stuffle, L. D., Olsen, R. C., and Garfield, N., *Bathymetry from Hyperspectral Imagery*, Master's Thesis, Naval Postgraduate School, Monterey, California, December 1996.

Wilson, T. and Davis, C., "Hyperspectral Remote Sensing Technology (HRST) Program and the Naval EarthMap Observer (NEMO) Satellite," paper presented at SPIE Conference on Infrared Spaceborne Remote Sensing VI, San Diego, California, July 1998.

INITIAL DISTRIBUTION LIST

1. Defense Technical Information Center..2
    8725 John J. Kingman Rd., STE 0944
    Ft. Belvoir, Virginia 22060-6218

2. Dudley Knox Library..2
    Naval Postgraduate School
    411 Dyer Rd.
    Monterey, California 93943-5101

3. Roland W. Garwood, Chairman...1
    Oceanography Department
    Naval Postgraduate School
    833 Dyer Road, Room 328
    Monterey, CA 93943-5122

4. Richard C. Olsen, Code PH/OS..5
    Physics Department
    Naval Postgraduate School
    833 Dyer Road, Room
    Monterey, CA 93943-5122

5. Pierre-Marie Poulain, Code OC/PN 2
    Oceanography Department
    Naval Postgraduate School
    833 Dyer Road, Room 328
    Monterey, CA 93943-5122

6. Newell Garfield, Code OC/GF..2
    Oceanography Department
    Naval Postgraduate School
    833 Dyer Road, Room 328
    Monterey, CA 93943-5122

7. Thomas M. Fisher...4
    P.O. Box 891176
    Temecula, CA 92589-1176

THIS PAGE INTENTIONALLY LEFT BLANK